Planning airborne photogrammetry and remote-sensing missions with modern platforms and sensors

Massimiliano Pepe, Luigi Fregonese & Marco Scaioni

View supplementary material

Published online: 11 Apr 2018.

Submit your article to this journal

View related articles

View Crossmark data

Taylor & Francis
Taylor & Francis Group

REVIEW ARTICLE

🔓 OPEN ACCESS   Check for updates

Planning airborne photogrammetry and remote-sensing missions with modern platforms and sensors

Massimiliano Pepe [a], Luigi Fregonese[b] and Marco Scaioni [b]

aDepartment of Sciences and Technologies (DIST), University of Naples "Parthenope" Centro Direzionale, Naples, Italy; bDepartment of Architecture, Built Environment and Construction Engineering (DABC), Milano, Italy

ABSTRACT

The mission planning in airborne Photogrammetry and Remote Sensing applications, depending on the system of acquisition and by the adopted platform (such as rotary and fixed wing aircrafts, glider, airship, manned or unmanned), is the first and essential step to ensure the success of a survey mission. The purpose of this paper is to provide an overview on mission planning techniques using passive optical sensors. The basic concepts related to the usage of the most common sensor technologies are described, along with the several possible scenarios that may be afforded by using modern airborne sensors. Several examples of flight plans are illustrated and discussed to highlight correct methods, procedures and tools for data acquisition in the case of different types of manned and unmanned airborne missions. In particular, the flight planning with more recent technologies of digital passive optical airborne sensors will be dealt with, including frame cameras and multi-/hyperspectral push-broom sensors. Furthermore, in order to ensure the complete success of an airborne mission, some up-to-date solutions to know in advance the weather conditions (cloud cover, height of the sun, wind, etc.) and the GNSS satellite configuration are illustrated.

Introduction

In the recent years the use of airborne optical sensors for photogrammetry and remote-sensing (PRS)[1] applications have been increasingly spreading out. This success is mainly due to the flexibility and the ability to gather high-resolution geometric data, also because of the impressive diffusion of Unmanned Aerial Systems (UAS) in the field of PRS (Clapuyt, Vanacker, & Van Oost, 2016; Colomina & Molina, 2014; Nex & Remondino, 2014). The use of such versatile and flexible platforms has led to a new and important revitalization of geodata acquisition from airborne platforms. Notwithstanding it is important to emphasize that manned and unmanned surveys have differences in several aspects, such as flight duration, ground coverage and data capture techniques; they share a common background. One of the major aspects is undoubtedly the use of digital cameras for imaging purpose, although the obsolete analogue cameras on manned aircrafts might be still employed in minor projects.

A detailed planning of a flight mission is a fundamental prerequisite for a successful acquisition of airborne data sets. This is due to the possible extension of the surveyed area and the fact the user does not have the direct control of the sensor, as in ground-based projects typical of close-range photogrammetry (Luhmann, Robson, Kyle, & Boehm, 2014) and terrestrial laser scanning (Shan & Toth, 2009; Vosselman & Maas, 2010). Given the definition of the products to be obtained from a flight mission and their technical requirements, the mission planning accounts for multiple steps that could be grouped as follows:

– Selection of a suitable sensor and platform;
– Flight plan design; and
– Analysis of the factors to be controlled during flight operations.

Each above-listed step should require an appropriate study in relation to the most recent platforms and sensors that are available for PRS applications. It is customary to divide the sensors into *passive* and *active* (Gomarasca, 2009). As known, the *passive* optical sensors may detect natural electromagnetic energy (radiation) that is reflected by the observed object (Aggarwal, 2004). Indeed, depending on the requirements of the specific application, there are sensors featuring different data acquisition geometry, format, geometric and radiometric/spectral resolution (including number, central

[1]In this context the term Photogrammetry refers to the extraction of geometric information from images, in particular for topographic mapping and 3D modelling; while with the term Remote Sensing a wider domain is addressed, including also the use of multispectral data for classification and photo-interpretation purpose.

wavelength and width of spectral bands), see Baltsavias (1999). *Active sensors* are based on the illumination of the surface to reconstruct by means of an electromagnetic signal that is reflected, returned and recorded by the sensor. The main types of active sensor technologies that are suitable to be installed on airborne platforms are: (i) LiDAR (Light Detection and RAnging – see Vosselman & Maas, 2010) or Airborne Laser Scanning (ALS), and (ii) microwave radar sensors (Wagner et al., 2007). It should be also mentioned that other technologies have been experimentally tried on UAS platforms (for instance, Time-of-Flight cameras, see Dorrington, Payne, & Cree, 2010), while new sensors, such as single-photon LiDAR's are now quickly developing (Degnan & Field, 2014) and are expected to gain a large market-share in the near future. As mission planning with such sensors may largely differ from the imaging systems, we omit to consider them in the analysis presented in this paper.

In order to describe in more detail the mission planning in PRS, it is convenient to analyse the passive optical sensors according to their data acquisition geometry, which is generally based on the *central perspective collinearity* (Kraus, 2007). Two main categories of camera systems can be distinguished: *frame cameras* and *line scanners imaging systems*. The former may be based on a *single-frame camera* consisting of a gridded network of elementary sensors, whose total size may reach a few hundred megapixels. The first technology that has been widely used for elementary sensors is Charge Coupling Device (CCD) (Toth, 2001). In recent years, the CMOS technology (complementary metal-oxide semiconductor – Neumann, Welzenbach, & Timm, 2016) has been quickly spreading out, because of the higher speed and the capability of controlling individual subportions of the whole sensor, despite of a larger noise. New types of sensors have been developed to overcome problems typical of CCD/CMOS sensors. For example, in FOVEON technology (Cheak, 2004), each elementary sensor may record all multiple spectral responses (e.g. red, green and blue channels in the case of RGB sensors), as each device is composed of three layers of elementary sensors. On the other hand, in CCD/CMOS sensing devices, each elementary sensor may record only monochromatic information. The composition of the elementary sensors in a pattern (e.g. following the Beyer scheme), lead to the possibility of recording multiple channels. However, interpolation is needed to complete the RGB content to be assigned to each pixel by using data from nearby elementary sensors. In addition, other technologies that may be considered as improvements of standard elementary sensors are now on the market, like eXcelon (Photometrics, 2017).

They generally output one type of radiometric information in the visible spectrum (RGB, panchromatic), but also some sensors are operating in near-infrared (see, e.g. Alba et al., 2011) or thermal infrared (Budzier & Garlach, 2011) wavelength. In the latter case, the sensor size is generally limited to few megapixels. Single-frame cameras are widely installed in UAS payloads due to their limited size and weight. In the group of frame-cameras, also *multi-frame imaging systems* have been developed for airborne photogrammetry, where large-format images are required for stereo-plotting. In such a case, several central perspective cameras acquire images that are then remapped and radiometrically fused to output a unique large format image (Neumann et al., 2016). Systems, including several single-frame cameras with different relative attitudes are today also quite popular to gather *oblique images* from multi-camera system carried by manned aircrafts, see Lemmens (2014). In *line scanner imaging systems* (also known, according to the old terminology, as "*push-broom*") the image is sequentially collected line-by-line as far as the aircraft is flying. In order to compose the final image, it is necessary to know six elements of exterior orientation (EO) per each scan line. Consequently, so many parameters may need to be solved for, requiring mandatory information about the position and attitude of the sensor during flight (Haala, Fritsch, Stallmann, & Cramer, 2000; Wang, Hu, Zhou, Li, & Zhang, 2013; Zhang, Hu, Meng, Yang, & Li, 2015).

Imaging sensors can be mounted on several airborne platforms, which are shortly reviewed in Subsection 1.1. Anyway, different categories of airborne cameras are used on specific platforms, being only single frame-cameras implemented in both manned and unmanned aircrafts. In the knowledge of the authors, up until today the multi-frame and line scanner imaging systems, as well as multi-camera systems for oblique imaging have been only used on manned platforms, since their size is still too cumbersome to allow the installation on the payload of UAS's. Moreover, sensors may be installed alone or in combination among them and with active sensors. For example, a manned aircraft may be equipped with a digital camera and a LiDAR sensor; a UAS may carry in the payload an RGB frame camera and a thermal camera; while other combinations are possible.

The existence of different sensors and platforms results in the fact that the planning a PRS aerial mission calls for a tailored approach according to the adopted equipment. Consequently, in this paper the up-to-date methodologies for flight planning depending upon different types of sensors are discussed. When possible, such as in the case of single-frame cameras, the use of manned and unmanned platforms is individually analysed. Flight missions for specific aims are considered as well, for example for sensor calibration. In "**Flight planning for frame camera missions**," the case of flight planning

for single-frame and multi-frame cameras is presented. The former ones are analysed from either manned or unmanned platforms. Oblique camera system is also investigated in "*Review of software for flight planning*". In "**Flight planning for line scanners sensors**," the key elements to build a flight plan for line scanner sensors will be discussed. In particular, three-line stereo cameras and hyperspectral sensors will be considered. In "**Data acquisition**," some aspects which are strictly connected with the flight plan are treated. In the pre-flight phase, several conditions that may influence the accuracy and quality of the final outputs need to be analysed (e.g. GNSS visibility planning and weather conditions forecast). During mission, the systems for management and control of flight planning are required in order of ensure a correct data acquisition and to enable the successive use of recorded information. Eventually, in "**Conclusions**" some conclusions are drawn and a tentative highlight of a few key-points for the future developing of flight mission planning are made.

The flight performance, classification and characteristics of fixed and rotary wing aircrafts are described in several publications (Filippone, 2008; Kemper, 2012; Yundong, Qiang, & Shaoqin, 2008). A review of some aircrafts that are frequently used for aerial survey in PRS projects is shown in Table 1.

Over the past decade, the applications of UAS for PRS has widely spreadout. The term UAS was adopted for the first time by the US Department of Defense and the Civil Aviation Authority (CAA) of the United Kingdom. This acronym is used to emphasize the fact that separate system components are required to support airborne operations without a pilot on board. A UAS is a system made up of the following main components: (i) the *Unmanned Aircraft Vehicle* (UAV), (ii) the payload, (iii) the human element, (iv) the control segment, (v) the data link (in general for small UAS is Wi-Fi type), (vi) and logistic support elements (Barnard, 2007; U.S. Department of Transportation, 2013).

The state-of-the-art of the application of UAS in PRS is reported in Colomina and Molina (2014). In this context, there are several classifications of UAS, according to the various characteristics of the aerial platform. A couple of interesting classification of UAS are that proposed in Eisenbeiss (2009) and Eisenbeiss and Sauerbier (2011) with respect to a larger set of parameters: powered and non-powered, heavier- or lighter-than-air, operational range, flight endurance, weather/wind dependency, and manoeuvrability (Table 2).

In the field of PRS, lots of UAS models are available. The continuous production of new models by companies and research institutes makes almost impossible to have an exhaustive list, that should always be incomplete. On the market, examples of fixed wing systems are the *Trimble UX5* (manufactured by Trimble), *eBee* (manufactured by senseFly, a Parrot Company) while as concerning rotary wing, some widespread models are the *MdMapper-1000* (manufactured by Microdrones) and ZX5 (manufactured by Trimble).

Flight planning for frame camera missions

Background

A key role in the formation of images on the passive sensors is played by the adopted optical system(s). For this reason, it is necessary to make a brief introduction on the concept of imaging through an optical system before illustrating the basic concepts for the

Table 2. Classification of UASs according to the classes unpowered and powered, as well as lighter or heavier than air, see Eisenbeiss (2009) and Eisenbeiss and Sauerbier (2011).

	Lighter than air	Heavier than air		
		Flexible wing	Fixed wing	Rotary wing
Unpowered	Balloon	Hang gliders Paraglider Kites	Gliders	Rotor-kite
Powered	Airship	Paraglider	Propeller Jet engines	Single rotors Coaxial Quadrotors Multi-rotors

Table 1. Characteristic of a few aircraft models which are typically use for aerial PRS missions.

Model	Manufactures	Type of wings	Max speed		Max altitude	
			(Kt)	(km/h)	(ft)	m
TECNAM 2006T	TECNAM	Fixed (high) wing	155	287	15,000	4572
Cessna Caravan	Cessna	Fixed (high) wing	185	343	15,000	4572
PARTNEAVIA P68 TC Observer	Vulcanair	Fixed (high) wing	220	407	20,000	6096
Piper PA-31 Navajo	Piper	Fixed (low) wing	227	420	25,000	7620
Gulfstream-III	Gulfstream Aerospace	Fixed (low) wing	442	818	45,000	13,716
Learjet 36	Gates Learjet Corporation	Fixed (low) wing	459	850	45,000	13,716
Bell 206L-4	Bell	Rotating wing	130	240	10,000	3048
Hughes 500E	MD Helicopters	Rotating wing	135	250	13,900	4236

construction of a flight plan in the case a frame camera is used. The image projection principle, which represents the ideal imaging process of a real object onto the sensor plane (and then in the image), is purely based on a geometric principle. By simplifying the assumption of Gauss and considering thin lenses (such as those used in cameras for PRS), the Huygens's equation becomes (Kraus, 2007):

$$\frac{1}{c} = \frac{1}{d_0} + \frac{1}{d_i} \quad (1)$$

where c is the focal length, d_0 is the distance between the object and the centre of the lens, and d_i is the distance between the image of the object and the centre of the lens (Figure 1). In the case d_0 is very large compared to c and d_i, the plane where the image is formed is practically coincident with the focal plane of the objective ($c \approx d_i$). The projective scheme that is realized is then a *central perspective*. Therefore, in the case of perfectly flat and horizontal terrain, the axis of the camera will be in *nadir* (or *vertical*) position and the scale of the image will be deduced from the relationship:

$$m_b = \frac{Z}{c} \quad (2)$$

being Z the *flying height above ground*. The angular coverage "seen" by the sensor is called *Field-of-View* (FoV). In the hypothesis of central perspective, it can be determined by the following formula:

$$\text{FoV} = 2 \cdot \text{arctg} \frac{p}{2\,c} \quad (3)$$

where p is the size of the sensor along the direction where the FoV is computed. As can be seen from Equations (2) and (3), the footprint on the ground of the image frame is closely connected to the relative altitude and the FoV. In the past, the preparation of flight planning for analogue film cameras was based on standard square photo format of size 230 mm × 230 mm. The standard focal length was 150 mm (wide angle camera), whilst the normal angle camera (300 mm) was adopted when it was necessary to fly at higher flying height above ground, for example, due to safety reasons or in the case of orthophoto production

for mitigating perspective distortions. As a consequence of the square sensor format, both FoV's along and across the flight line (FL) were the same. While in old analogue cameras the knowledge of the focal lens was sufficient to make a flight plan, in modern *digital aerial cameras* (DAC) the combination of focal length, pixel size (usually square) and the sensor format determines its operational profile. In fact, in DAC's these parameters may differ from one camera prototype to another. The most important parameter is now the *ground sampling distance* (GSD), which is calculated with the formula (Neumann, 2005):

$$\text{GSD} = \frac{Z}{c} \cdot \text{CCD pixel size} \quad (4)$$

To investigate how the flight planning parameters change for each sensor, four frame DAC's of various format are considered in Table 3 (Grenzdörffer, 2010; Höhle, 2011). In the upper part, the intrinsic properties of the sensor are listed, while the lower part shows some parameters of the flight plan designed to obtain a GSD = 10 cm. For instance, the flying height above ground ranges from 938 m to 2000 m.

To compute the *absolute height above sea level* (ASL) of the flight, it is necessary to know the height of the terrain, or better the average height above ground level (AGL). Several regional and global DTM's are today available to compute AGL. Therefore, once the height of the terrain and the flying height above ground necessary to guarantee a given GSD is known, it is possible to calculate the ASL by the following formula:

$$\text{ASL} \equiv H = Z + \text{AGL} \quad (5)$$

It is important to emphasize that in projects where a high geometric resolution is required, as in the case of UAS surveys, global DTM's (e.g. SRTM from NASA, see Jarvis, Reuter, Nelson, & Guevara, 2008) may not be able to provide a sufficient accuracy in the AGL estimation.

Results from Equations (4) and (5) should be considered as average values because the conditions set out above cannot perfectly met due to sloping terrain (main reason), changes in flight altitude, etc. The footprint of each frame in the direction of the aircraft's motion is called "*covered size along FL*",
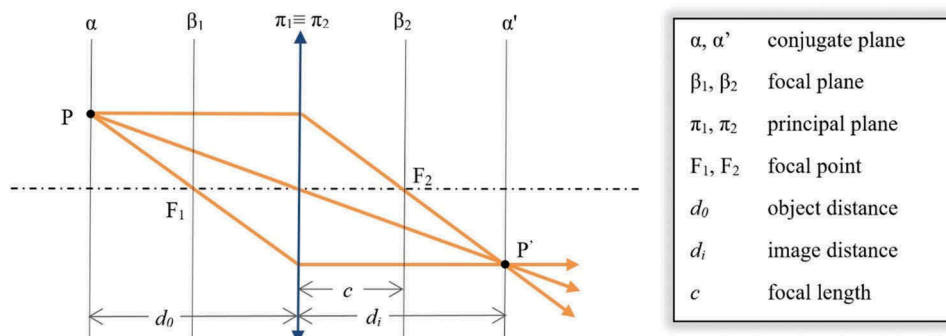

Figure 1. Image formation by a converging lens.

Table 3. Flight planing parameters of four DAC's required to obtain a GSD = 10 cm.

	DMC II 250 (Jacobsen, 2010)	UltraCamEagle 80 mm (Microsoft, 2016)	PhaseOne iXU 1000 50 mm (Phase One Ind., 2016)
Sensor geometry			
Pixelsize (μm)	5.6	5.2	4.6
Focal length (mm)	112	80	50
No. of pixels along flight line	14,016	13,080	8708
No. of pixels across flight line	16,768	20,010	11,608
Results			
Height above ground (m/ft)	2000/6562	1538/5047	1087/3566
Sensor size along flight line (mm)	78	68	40
Sensors size across flight line (mm)	94	104	54
FoV along flight line	39°	46°	44°
FoV across flight line	46°	66°	56°
Footprint along flight line (m)	1466	1308	870
Footprint across flight line (m)	1722	2000	1160

while the one in perpendicular direction is referred to as "*covered size across FL*". It should be emphasized that such a covered size, both in the longitudinal and transverse direction, is consistently linear only in the case the terrain is flat.

Traditional flight planning for stereo-photogrammetry

The acquisition of the same scene from two different points of view, and more precisely, by at least two metric photographs, allows a stereoscopic 3D vision. The distance B between the perspective centres of two consecutive photos in the sense of the aircraft's motion, is called *baseline*. By varying the length of the baseline different *longitudinal* (i.e. along the direction of FL) *overlaps* – or *endlaps* – may be obtained. Traditional values of overlap range from 60% to 80% (Mikhail, Bethel, & McGlone, 2001). An overlap of 80% is typically selected in city centres to better penetrate into urban canyons. In the traditional approach (or normal case), the theoretical accuracies ($\sigma_{X,Y}$) along both axes (X,Y) that are approximately parallel to the ground is given by (Kraus, 2007):

$$\sigma_x = \sqrt{\left(\frac{\xi}{c} \cdot \frac{Z}{c} \cdot \frac{Z}{B} \cdot \sigma_{p_\xi}\right)^2 + \left(\frac{Z}{c} \cdot \sigma_\xi\right)^2} \quad (6a)$$

$$\sigma_y = \sqrt{\left(\frac{\eta}{c} \cdot \frac{Z}{c} \cdot \frac{Z}{B} \cdot \sigma_{p_\xi}\right)^2 + \left(\frac{Z}{c} \cdot \sigma_\eta\right)^2} \quad (6b)$$

where, σ_ξ and σ_η are the estimated precisions of the image coordinate (ξ,η) measurements, $\sigma_{p\xi}$ is the precision of parallax measurement, Z is the relative flying height above ground, c is the principal distance of the adopted camera, and B is the baseline between consecutive perspective centres. The theoretical accuracy (σ_Z) along the vertical direction (Z) can be defined as:

$$\sigma_Z = \frac{Z^2}{c \cdot B} \cdot \sigma_{p_\xi} \quad (6c)$$

Equations (6a)–(6c) show that since B and c are constant, the errors along Z increase in proportion to the square of the distance Z. Therefore, if B is small compared to Z, the intersection of corresponding rays will be weak and thus the accuracy in the viewing direction quite poor (Kraus, 2007). In other words, the larger the longitudinal overlap, the higher the error along Z component.

A practical aspect that may control the correct stereoscopic acquisition of two consecutive frames is the acquisition time. Indeed, in aerial surveys an import role is taken by the *frame rate* and the *shutter speed*. The former refers to the number of individual frames that the adopted DAC may acquire per unit time (usually it is expressed in "frames-per-second" – FPS). For example, the large frame DAC UltraCamD produced by Vexcel Co. offers a frame rate of more than 1 FPS (Kremer & Gruber, 2004; Luhmann, Robson, Kyle, & Boehm, 2013). Each sensor has its own frame-rate value. The shutter speed refers to the amount of time that each individual frame is exposed for. Frame rate and shutter speed impose the minimum time required to shoot two consecutive frames. Once the longitudinal overlap is fixed, the higher the relative height, the longer the shooting interval. The setting of these two parameters (frame rate and the shutter speed) is very important especially in low altitude flights or in flight plans with large overlaps.

A sequence of photos acquired along the same FL is generally addressed to as "strip". Stereo-plotting is usually operated on two consecutive frames belonging to the same strip, whose images should feature similar characteristics (Z and longitudinal overlap). Moreover, the three relative orientation angles between consecutive photos have to be very small (a few degrees). In aerial missions this condition is usually required by limiting the absolute values of w and j angles, which express the parallelism between the photo and the ground. Given the baseline and the footprint of the frame along the FL (S), it is possible to calculate the longitudinal overlap (as a percentage) by the following formula (Grubera, Perkob, & Ponticellia, 2004):

$$\text{overlap} = \frac{S - B}{S} 100 \qquad (7)$$

The geometric layout of the resulting strips depends on the structure of territory to survey and the shape/extension of the area of interest (AOI). We limit here to recall the basic configurations, while the reader may find more details in the photogrammetric handbooks (e.g. Kraus, 2007; Mikhail et al., 2001). The first one is based on *corridors*, that consists of single strips following the longitudinal axis of the main target object of the survey. Corridors are used in the case of objects having a prevalent linear extension, such as rivers, transportation corridors, power lines, etc. An example of flight planning in the case of corridors is sketched in Figure 2 (a). When the width of a single strip cannot entirely cover the AOI, it is necessary to fly several parallel strips to compose a full *photogrammetric block* (see Figure 2 (b)). The overlap between adjacent parallel strips (*sidelap*) usually range from 20% to 30%, in relation to the morphology of the survey area to guarantee a safe minimum coverage to avoid gaps in stereo-plotting: a smaller *sidelap* is needed on flat areas, a larger one on steep terrains. In some projects, the use of larger overlaps (up to 60%) results in strengthening the block geometry, since a larger number of well distributed tie points are likely to be extracted in *automatic aerial triangulation* (Heipke & Eder, 1998). The distance between two FLs is called *line spacing* (SP) or sometimes *run spacing*. This can be calculated, known the image coverage across FL (W) and the required *sidelap* by using the following equation:

$$\text{SP} = W \cdot \left(\frac{100 - \text{sidelap}}{100} \right) \qquad (8)$$

In general, such large "blocks" are tentatively designed using parallel strips, but a more involved design might be called for in the case of complex topography. In addition, a photogrammetric block may also include some transversal strips, for example at the ends of the regular parallel strips (*closing strips*). This configuration also reinforces the block geometry and allows a considerable reduction of the

ground control points (GCP) to be measured on the ground (Ebadi, 2006; Kraus, 2007).

Several studies have been published on the properties of photogrammetric blocks and corridors depending on their characteristics: for example, point precision (Kraus, 2007) and inner/outer reliability (Förstner, 1985). The use of Global Navigation Satellite System/Inertial Measurement Unit (GNSS/IMU) assisted aerial triangulation (Cramer, 2003) or direct GNSS/IMU positioning (Madani & Mostafa, 2001; Mian et al., 2015), which are nowadays consolidated approaches, may help simplify the requirements in term of block structure and ground control. Consequently, the main issues that should be considered during flight planning are the respect of relative flight heights to obtain the required photo-scales for the project, and the stereoscopic coverage of the AOI. Planning a flight mission in the case of flat terrain is then relatively simple. Otherwise, two methods can be used.

In the first one (probably the most popular), each strip has its own altitude in relation to the height of the terrain (Morgan & Falkner, 2001). The ASL is calculated by Equation (5) and the range of the actual relative altitudes determines a minimum and maximum GSD's. These values, depending on the characteristics of the project, determine the quality criteria of the flight plan. In this configuration, it is important to check out the variation of GSD in the areas at lower altitudes to ensure that the variation of GSD within the strip does not significantly exceed the "project" GSD. In addition, it is also necessary to analyse the correct stereoscopic coverage of the entire AOI.

The second planning mode is called *terrain-following* (Möllney & Kremer, 2013). It consists of maintaining a relatively constant altitude AGL during the flight. Of course, an accurate terrain model is required to design a flight plan by using this approach, which has several advantages, among which a more uniform spatial resolution along the FLs and fewer problems in respecting planned sideward and forward overlaps.

The main disadvantages are related to the altitude change, which may involve a significantly increased
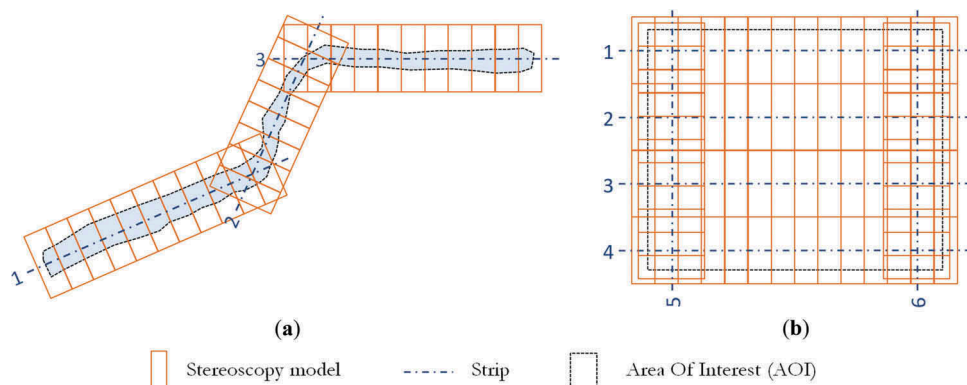

Figure 2. Example of a flight plan design for "corridor" mapping (a) and for a photogrammetric block (b).

workload for the pilot and possibly major problems to obtain the permission to fly by the aeronautics authority. The *terrain-following* approach is largely valuable in UAS projects and sometimes, even in mountainous area for standard flights.

Review of software for flight planning

The software for flight planning is provided by sensors' manufacturers or by independent commercial and non-commercial developers (see Table 4). Also open-source software packages have been developed, for example Mission Planner that can be used for planning UAS missions (Oborne, 2013; Thomas & Gray, 2016). Furthermore, some pieces of software are specifically designed for a type of platform, as Z/I Mission for DMC camera and in the case of several UAS's, while others have a general applicability.

In order to create a simple and intuitive environment for the construction of a flight plan, the most recent version of some software packages enable users to work in GoogleEarth™ environment. Also, once the AOI has been identified and defined by drawing a polygon, the software allows to automatically calculate the necessary FLs.

In the following, three examples of flight planning for mapping purpose based on frame-camera sensors are reported. The first case concerns a photogrammetric block on the Ischia Island (Italy) using UltraCam X sensor (manufactured by Vexcel Imaging GmbH, Austria). The constructive characteristics are: pixel size = 7.2 μm, focal length = 120 mm, image format 14,430 pixels across track and 9420 pixels along track. The flight plan has been built with Topoflight 3D Flight Planning Software to obtain a GSD = 10 cm (see Figure 3). To check whether the flight plan fulfils the project specifications, Topoflight creates a "*Quality Control Map*" that shows the GSD values within the AOI.

Another example of flight planning concerning a case of road survey (corridor mapping) was obtained by *Z/I Mission* software, which was developed for Z/I DMC sensor (pixel size = 12 μm,

focal length = 120 mm, image format 13,824 pixels across track and 7680 pixels along track). The purpose of the project was to create a flight plan with an average GSD = 10 cm. The flight plan consisted of three strips with longitudinal overlap of 60% and relative flying height of 1000 m. Given as input the desired GSD and determined the flight altitude above the ground, it was necessary to calculate the absolute altitude flight. This value could be obtained by the average altitude of the terrain. In Figure 4 (right side) the terrain profile in correspondence of the strips' axes are shown.

The last example of flight planning for a frame camera was carried out by *Mission Planner* (open source) software (Planner, 2016) over a dam in Italy (Figure 5). The aerial platform chosen was a quadcopter UAS with a flight speed of 12 m/s. The mission planning was designed for a Canon EOS5markII SLR camera (Canon, 2016) equipped with a 15 mm lens in order to obtain a pixel size of about 2cm. The relative flying height was 40 m, while the values of longitudinal overlap and sidelap were 60% and 50%, respectively. The green markers in Figure 5 represent the "waypoints" where images were supposed to be shot, while the red line bounds the AOI.

Flight planning for misalignment calibration using frame-camera sensors

As already introduced, the direct measurement of sensor orientation parameters (position and attitude) makes easier and speeds up the processing workflow of frame-camera sensors.

Furthermore, in the case of line scanner sensors, the knowledge of the EO parameters is mandatory for data acquisition. The EO is obtained with the integration of GNSS and IMU sensors (Mostafa, 2001). This coupling merges the long-term stability of GNSS differential positioning and the short-term precision of IMU, which also may determine camera rotations. The features and performance of some GNSS/INS navigation systems are reported in Schiele, Kleusberg, and Horn (2002) and Rizaldy and

Table 4. Popular software packages for flight planning.

| Software	Manufacturer	Platform
Z/I Mission	Intergraph® Z/I Imaging®	Aircraft
SnapPLAN	Track'Air/Lead'Air	Aircraft/helicopter/UAS
IGIplan	IGI mbH	Aircraft/helicopter/UAS
Topoflight 3D Flight Planning Software	Developed by TopoFlight Systems and distributed by New Tech Services, Inc	Aircraft/helicopter/UAS
Mission Planning	Icaros	Aircraft/helicopter/UAS
Airborne Scientific Flight Planner	Airborne Scientific, Inc	Aircraft/helicopter
Leica Mission Pro	Leica Geosystems	Aircraft/helicopter
Optech FMS Planner	Teledyne Optech	Aircraft/helicopter
Aibotix AiProFlight	Aibotix GmbH	UAS
Mission planner	SPH Engineering	UAS
Mission Planner	Created by Michael Oborne for the ArduPilot open source autopilot project	UAS
Trimble Access™ Aerial Imaging	Trimble UAS	UAS
Emotion	SenseFly (Parrot company)	UAS
MAVinci	MAVinci GmbH	UAS
Pix4Dcapture	Pix4D	UAS
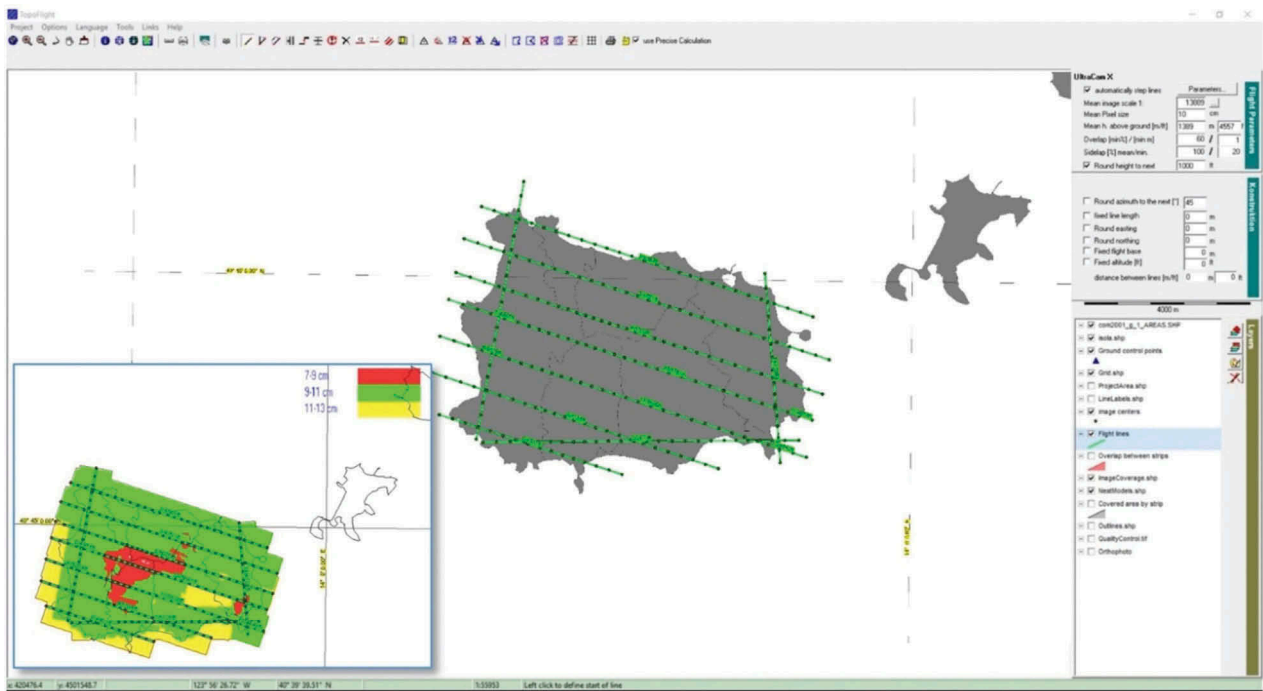
Figure 3. Example of a photogrammetric block planned over Ischia Island (Italy) using TopoFlight software. In the bottom-left corner, the "Quality Control Map" is displayed, which shows the values of GSD, which are obtainable in the different parts of the AOI (depicted in different colours).
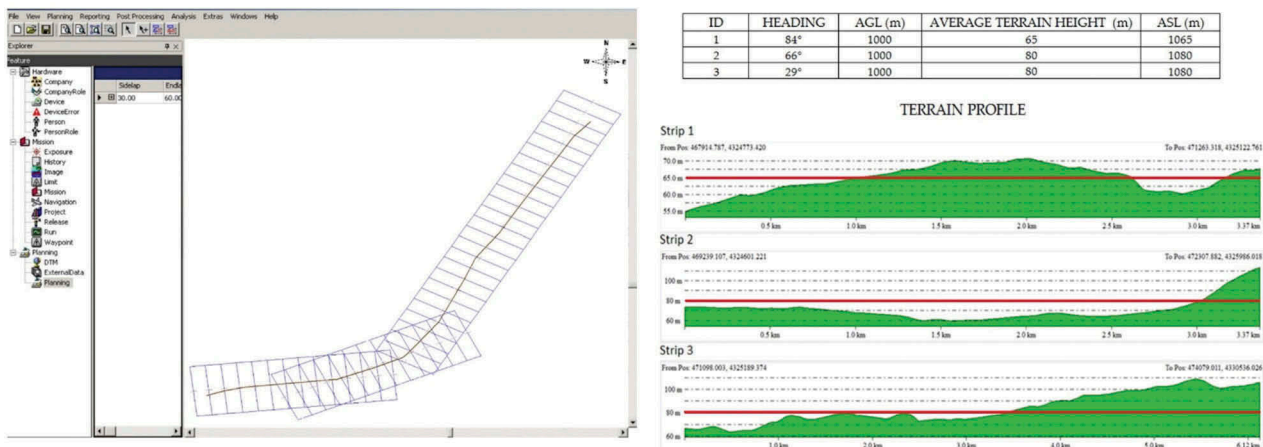

Figure 4. Example of corridor flight planning for the frame DAC DMC obtained with Z/I Mission software (on the left), and three terrain profiles along the axes to the strips (on the right). The red lines indicate the average flight height chosen for the flight plan.

Firdaus (2012). To obtain the positional accuracy required to meet the standards of certain mapping products, *differential* GNSS techniques are usually adopted. These require a "master" GNSS station on the ground. Using a single "master" station cannot be sufficient in some aerial survey projects spanning over a large AOI, as the long distance from it may dramatically reduce the accuracy of positioning. Placing multiple GNSS "master" stations is an option that sometimes could not be viable in remote or inaccessible locations. To overcome this difficulty, the availability of Continuously Operating Reference Stations (CORS) as "virtual master" stations for airborne GNSS surveys (Mostafa, 2002) makes possible

to process the entire trajectory with sufficient accuracy.

The mathematical equation that connects GNSS/INS system with the imaging sensor is (Cramer, Stallmann, & Haala, 2000; Schwarz, 1996):

$$\Delta r^m(t) = r^m(t) + s \cdot R^m_{\ b}(t) \cdot p^b \qquad (9)$$

where:

$\Delta r^m(t)$ position vector of an image object in the mapping frame (m);

r^m coordinate vector from the origin of the mapping frame to the centre of the positioning sensors on the aerial platform,

Figure 5. Flight planning realized by Mission Planner software for a quadcopter UAS mission.

given in the *m*-th frame (to be determined from calibration);

$R^m{}_b(t)$ spatial 3D rotation matrix from the aircraft body frame (*b*) into the mapping frame (from GNSS/IMU);

s scale factor depending upon the relative height of the sensor;

p^b vector of image coordinates given in the *b*-th frame.

In general, the determination of r^m vector requires the boresight misalignment angles between camera and IMU. This task is obtained through a calibration procedure requiring a specific flight plan (Wegmann, 2002). A proper calibration field over a non-flat terrain and with abundant and regular distribution of accurate GCP's is needed. The approach to determine these angles is to investigate the IMU error in several directions (see Figure 6(a)). Let be *X* the direction of the flight, *Y* the orthogonal axis in the horizontal plane, and *Z* the vertical direction (positive downwards). The boresight error can be decomposed as follows:

- *roll error*: angular misalignment between IMU and camera around the *X* axis;
- *pitch error*: angular misalignment between IMU and camera around the *Y* axis; and
- *heading error*: angular misalignment between IMU and camera around the *Z* axis.

To determine all these misalignments an accurate flight planning including the following characteristics has to be implemented:

- opposing FLs allow to determine the roll error;
- opposing FLs at two different altitudes allow to determine the pitch error; and
- crossing FLs allow to determine the heading error.

An example of photogrammetric block for misalignment calibration purpose has been designed by *Z/ I Mission* flight planning software for *Z/I DMC* sensor integrated to IMU Applanix POS-AV510 (Neumann, 2004). It consists of nine strips (five strips regular and four cross-strips) at altitude of 800 and 1500 m with longitudinal overlap of 60% and sidelap of 30%, respectively (see Figure 6(b)).

In a region where the anomalous gravity field is relevant, it is necessary to modify Equation (9) to take this phenomenon into account. Indeed, recent studies about the impact of the anomalous gravity field in GNSS/INS applications (Barzaghi, Carrion, Pepe, & Prezioso, 2016) have shown that neglecting the impact of the Deflection-of-Vertical (DoV) in aerial surveys induces horizontal and vertical errors in the measurement of an object that is part of the observed scene, which might vary from a few tens of centimetres to over 1 m. To improve the accuracy of the GNSS/INS approach, a corrective rotation matrix may be introduced in Equation (9) to account for the transformation from the local level frame to the ellipsoidal frame (Pepe, Prezioso, & Santamaria, 2015).

Over the last few years, direct georeferencing has also been applied to UAV platforms. However, the biggest challenge for using GNSS/INS sensors on this type of platform is the adaptability of these sensors to UAV platforms, especially small ones. In this way, thanks to lower price, smaller requirements and much lower energy consumption, MEMS (micro-electro-mechanical sensor) technology has become interesting. Currently, taking into account technological development and suitable algorithms, the achievable precision is few centimetres in position and better of 0.5° in attitude (Eling, Klingbeil, & Kuhlmann, 2015).
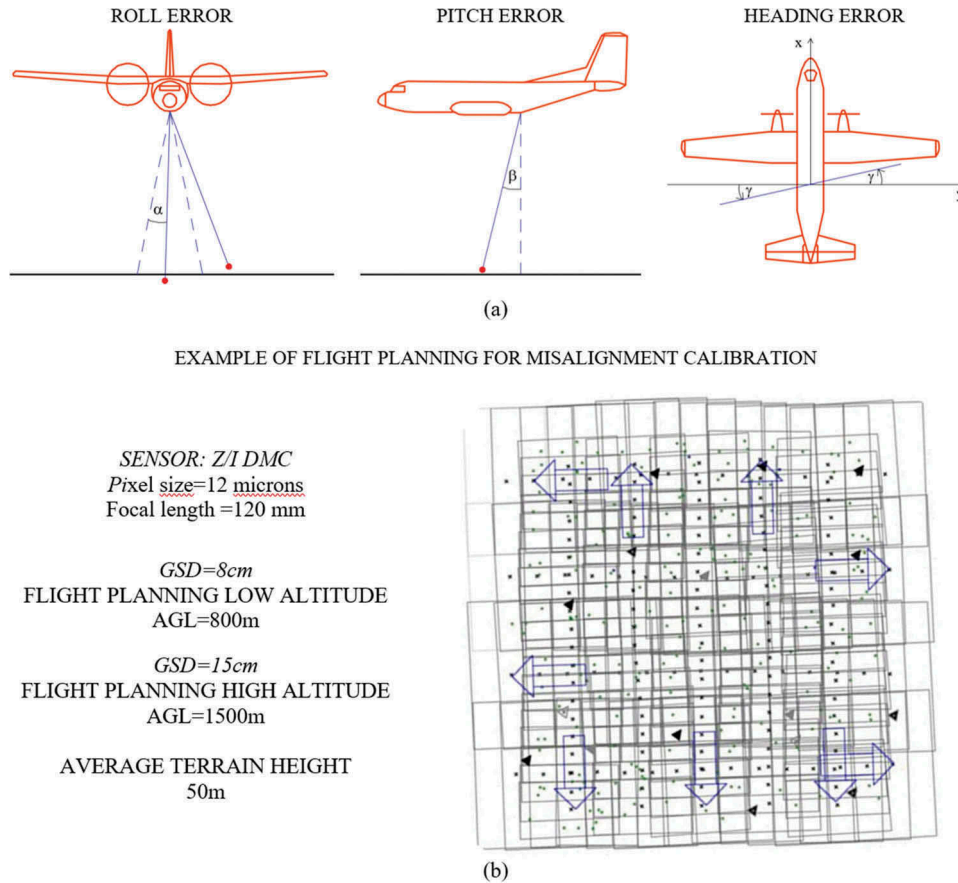
Figure 6. Flight plan for boresight calibration: decomposition of boresight error (a); flight plan for misalignment calibration of a frame DAC (b).

Digital oblique-frame cameras

In recent years, aerial photogrammetry has increasingly been using frame imaging systems able to capture nadir and oblique images at the same time. The actual oblique camera systems come in a variety of configurations, which differ in the sensors number, format, arrangement of multiple sensors, mode of acquisition and spectral sensitivity (Rupnik, Nex, & Remondino, 2014).

An example of oblique camera system is Leica RCD30 Oblique Penta System, which consists of five cameras: four cameras inclined at 35° and along four orthogonal directions, and one nadir-looking camera. Other examples of oblique camera system are MIDAS made by TrackAir company (Madani, 2012), IGI DigiCAM Penta (Jacobsen & Gerke, 2016), and Pictometry Vexcel Osprey (Gruber & Walcher, 2014). The shape of the ground coverage captured simultaneously by the five cameras looks like a "Maltese Cross" (Petrie, 2009). In such a configuration, the formula for GSD calculation is reported in Höhle (2008; 2011) and recalled here:

$$\text{GSD} = \text{pixelsize}' \cdot \frac{Z}{c} \cdot \frac{\cos(\beta - t)}{\cos \beta} \qquad (10)$$

where β is the angle between the direct line from the lens to a target and the vertical, while t the tilt angle of the considered camera.

In the case of nadir and oblique acquisition, GSD will depend upon the camera position (Pepe & Prezioso, 2016). However, flight planning made for oblique camera systems (designed as a frame camera) are realized on urban areas at relatively low altitudes, with a GSD which varies from 3 cm to 15 cm and, in these situations, there will be a small difference between GSD acquired in nadir and oblique images.

An example of flight planning acquired by Leica RCD30 Oblique Penta System on the Nöllen area (Switzerland) is shown in Figure 7. It consists of six strips (625 images) at 5 cm average GSD with 30% of sidelap and 60% of longitudinal overlap.

Frame camera using Structure-from-Motion (SfM) approach

The image orientation based on the so called "*Structure-from-Motion*" (SfM) approach has become quite popular in close-range photogrammetry. Indeed, in such a type of projects no support is generally provided by GNSS/IMU sensors. Furthermore, the shape of objects to survey may
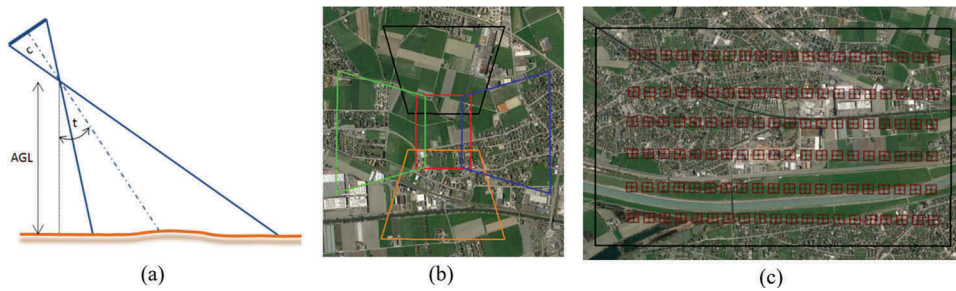
Figure 7. Acquisition scheme in oblique camera (a); footprint of penta-oblique system (b); flight planning (waypoints) on GoogleEarth™ map (Nöllen area – c).
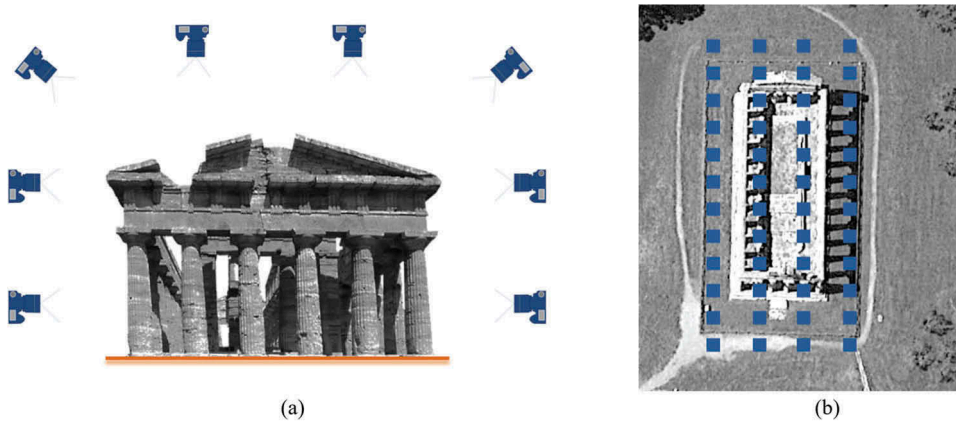

Figure 8. Example of the flight planning for a UAV sensor (MD4-1000 multicopter).

require a very involved geometry for photogrammetric blocks, also including several convergent images. SfM may solve for camera EO in a fully automatic manner, without any a priori knowledge of the approximate positions for cameras and 3D points (Snavely, 2008; Westoby, Brasington, Glasser, Hambrey, & Reynolds, 2012). In the case the block geometry is adequate, camera calibration parameters may also be estimated within the bundle adjustment that is integrated into the SfM pipeline, whose core is the automatic extraction and robust matching of corresponding features from a set of multiple overlapping images (Barazzetti, Forlani, Remondino, Roncella, & Scaioni, 2011; Barazzetti, Remondino, & Scaioni, 2010). SfM requires a block of images with a high degree of overlap that capture the complete 3D structure of the scene viewed from several locations. As the complex geometry of the objects that may be surveyed using SfM, it is difficult to decompose the analysis of the expected precision in the parallel and orthogonal directions (see Equations (5)(bis) and (6a)–(6c)) with respect to the photo plane, such in the case of normal configuration. The standard error $\sigma_{X,Y,Z}$ of the X, Y and Z object coordinates of a generic 3D point

may be evaluated by the following relation proposed in Fraser (1996):

$$\sigma_z = \frac{q \cdot Z}{c\sqrt{k}} \cdot \sigma_{p_\xi} \qquad (11)$$

where k is the number of images used to determine the same point and q is a design factor expressing the strength of the camera network; it is basically dependent on the angles between intersecting homologous rays and on the baselines. By looking at Equation (11), the accuracy of the acquisition scheme significantly improves with the increase of convergent images and the total number of images. A comment should be made about the relevance of the baselines' length, which plays a primary role in the determination of precision along Z direction in the case of stereo configuration (see Equation (6c)). Under a geometric point-of-view, longer baselines improve the spatial intersection of homologous rays (El-Hakim, Beraldin, & Blais, 2003). On the other hand, shorter baselines result in less relevant differences in the image content, because the perspective deformations are not too much emphasized. This similarity of the image content may help the image matching algorithms adopted for automatic image orientation and successive dense matching for surface reconstruction. Consequently, the best results

may be obtained thanks to a trade-off between both factors, to be defined case-by-case.

The SfM approach has become very popular in UAS projects, whose characteristics are very often close to the ones of close-range photogrammetric projects. Thus, the preparation of a flight plan for a UAS mission should take into consideration the parameters mentioned above. In order to report a typical example of such applications, the flight plan for a survey of a Greek temple in the archaeological site of Paestum, Italy (see Figure 8) using a MD4-1000 multicopter UAV (max payload of 1.2 kg) (see Microdrones, 2017) and the software mdCockpit (Mesas-Carrascosa, Rumbao, Berrocal, & Porras, 2014) is presented here. The main characteristics for this project are: 60% of sidelap and 80% of endlap for nadir photos and in oblique strips with a tilt angle of 45°; flight altitude ASL = 88 m to obtain a GSD = 3 cm. The frame-camera sensors chosen for the project were the Olympus E-P1 camera (12 Megapixels, 4 μm pixel size) with 17 mm focal length for the oblique images, and the Olympus XZ-1 (10 Megapixels, 2 μm pixel size) with 6 mm focal length for the nadir and lateral images.

Flight planning for line scanners sensors

Background

The alternative technology for image acquisition is based on linear sensors that passively record the electromagnetic response from the ground and object surface. Such linear sensors may move and scan extended areas. According to the acquisition mechanism, two types of sensors can be distinguished: *whisk-broom* (scanner across-track) and *line scanners* (scanner along-track) sensors (Fowler, 2014). Before briefly reviewing both technologies, two important issues should be generally addressed. As the imaging process is operated in dynamic way, the integration with a GNSS/IMU unit for direct positioning is mandatory for all types of linear sensors. Secondly, since the installation of independent multiple linear sensors is quite simple, several cameras have been developed for the acquisition of multi- and hyper-spectral imagery. On the other hand, the linear cameras have been implemented for decades in spaceborne imaging systems for remote-sensing applications. Consequently, the ones implemented in airborne platforms may have benefited from the experience achieved with satellite sensors.

Across-track/whisk broom sensors scan the ground following a series of lines that are perpendicular to the motion direction of the sensor platform. Each line is scanned from one side of the sensor to the other, using a rotating mirror. Along-track push-broom scanners also use the forward motion of the platform to record successive scan lines that are perpendicular to the flight direction. In this way, a two-dimensional image

can be derived (Kumar, 2005; Ringaby et al., 2014). The former technology is quite popular in ALS active sensors, but is today scarcely applied for passive imaging. On the other hand, the latter technology has gained popularity in aerial photogrammetry, due to the possibility of collecting long-format images to be used for both stereo-plotting and orthoimage production. For this reason, this type of linear sensor will be focused in-depth in the following subsection.

GSD calculation with line scanners sensors

In the line scanners sensors, the speed of the aircraft is of great importance for the evaluation of GSD. Indeed, to record contiguous scan lines, it is necessary to find the optimum *ground speed* of the aircraft (G_S), that is the relative velocity with respect to the ground. This may be obtained from the knowledge of aircraft's velocity relative to the atmosphere (*air speed – A_S*) and the wind speed (V_W). The following vectorial relationship (Mallaun, Giez, & Baumann, 2015) can be written:

$$\vec{G}_S = \vec{A}_S + \vec{V}_w \qquad (12)$$

The GSD *along-track* ($GSD_{al\text{-}tr}$) direction can be obtain as (Semanjski, Dubravko, & Hrvoje, 2008):

$$\text{GSD}_{al-tr} = G_S \cdot T_I \qquad (13)$$

where T_I is the *integration time*, i.e. the time needed to collect a single scanline. The integration time is positively correlated with both the number of spectral bands and the number of viewing directions of the camera (Dell'Indice, 2008). The GSD *across-track* ($GSD_{Ac\text{-}tr}$) in the orthogonal direction to the flight motion is related to the focal length (c), the sensor unit size (p) and the relative flying height (Z):

$$\text{GSD}_{ac-tr} = \frac{Z}{c} \cdot p \qquad (14)$$

A flight mission to be operated with a line scanners camera is typically made up of a set of FLs. The analogue concept of the frame footprint in the case of frame DAC's is replaced by the footprint along the acquisition line. Because of the possible different GSD in across- and along-track directions, to limit the GSD to a prefixed value it may be necessary to fly at multiple heights, whose variation may become really important when using long focal lengths (Table 6). In addition, because the survey accuracy in line scanners sensors is closely related to the GNSS/IMU system, the calibration step is very crucial. The flight planning for misalignment calibration with line scanners sensors may be operated in the same way as the one for frame cameras (see Sect. 2.1.1): the flight planning contains four strips (two regular and other two rotated of 90° with respect to the previous ones) at low altitude and other four

strips (positioned such as the ones at lower altitude) at a higher altitude.

Three-line stereo line scanners

In the imagery process in *three-line scanners*, each scan line provides information about the objects on the ground from different viewing angles assembled into strips, as shown in Figure 9(a). These sensors generate overlapping forward, nadir- and backward-pointing strip images that allow the production of stereoscopic models, DEM's and orthorectified images for mapping purposes (Grun & Zhang, 2002). Additional linear arrays can also be incorporated into the scanner focal plane to allow multispectral, colour and false-colour images to be generated (Petrie & Walker, 2007).

Some popular three-line stereo line scanners used in airborne mapping projects are: Leica Geosystems ADS80 (Bühler, Marty, & Egli et al., 2015), Leica ADS100 SH100, 3-DAS-1 (Wehrli, Gayda, Wehrli, & BeThel, 2004) and JAS 150 Jena Airborne Scanner (Georgi, Stognienko, Knuth, & Albe, 2005). In Table 5 some parameters for flight planning to obtain a maximum GSD = 10 cm when using these three sensors are reported. Obviously, the GSD in across-track direction obtained with Equation (14) must be verified with the GSD along the direction of flight.

This latter parameter is closely linked to the acquisition speed of the aerial platform.

An example of mission planning using sensor ADS80 has been obtained with Leica Geosystems *MissionPro*. Here the aim was to achieve a GSD between 12 cm and 20 cm on a photogrammetric block to be flown in the south of Sardinia, Italy (see Figure 9(b)). Beyond of this solution that has been developed by using the Leica Geosystems proprietary software, other common packages might be alternatively used, such as, for example, *Topoflight* or *IGIplan-Mission Planning*.

Hyperspectral line scanners sensors

Hyperspectral sensors are passive sensors widely used for remote-sensing applications in forestry, agriculture, environmental and urban sciences. These may entail the classification of vegetation species, the analysis of water quality, coral reefs and wetlands, the recognition of toxic materials and waste deposits (Cocks, Jenssen, Stewart, Wilson, & Shields, 1998; Van der Meer et al., 2012; Varshney & Arora, 2004).

A hyperspectral line scanners sensor consists of an optical system projecting an image onto a linear array of sensors, typically a charge-coupled device (CCD) array. This spectral data is generated using a dispersive prism or grating that acts as an imaging spectrometer
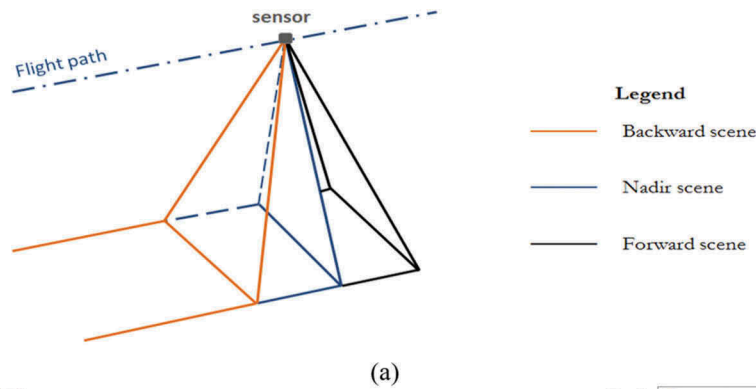
(a)
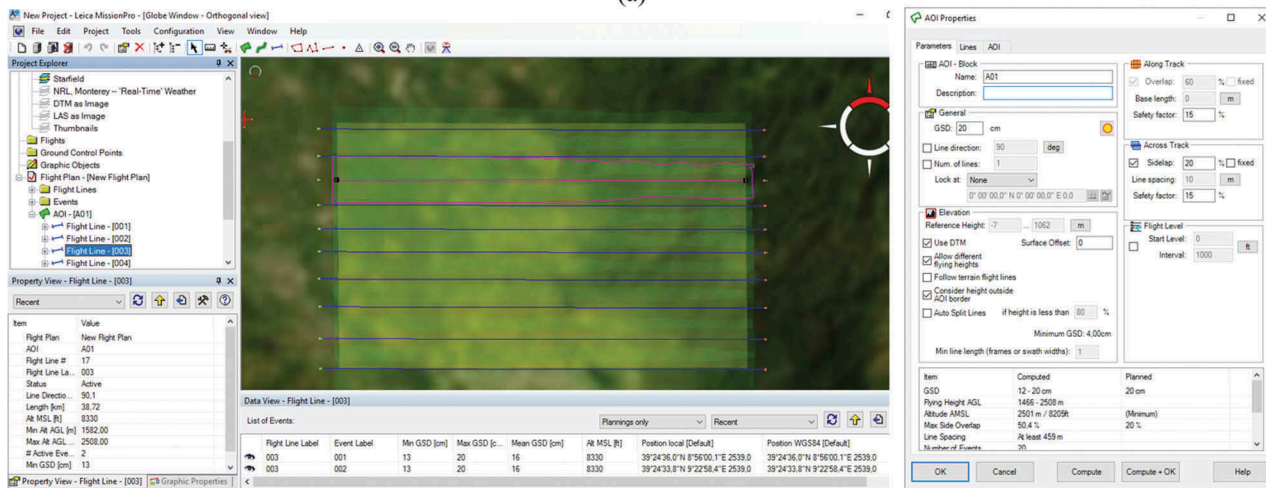
(b)

Figure 9. (a) Basic image-acquisition scheme of a typical three-line stereo push-broom scanner; (b) flight planning with Leica MissionPro software.

Table 5. Flight planning parameters to obtain a maximum GSD = 10 cm (considering a ground speed of 110 km) are listed for three popular three-line stereo scanners.

	ADS80	ADS100-SH100	3-DAS-1	JAS 150
Sensor geometry				
Pixel size (mm)	6.5	5	9	6.5
Focal length (mm)	62.5	62.5	110	150
No. pixels across-track (pixels)	12,000	20,000	8000	12,000
Minimum exposure time (ms)	1	0.5	1.4	1.25
Parameters for flight planning				
Flying height above ground	962 m/3155 ft	1250m/4101 ft	1222 m/4010 ft	2307 m/7568 ft
FoV across-track	64°	65.2°	36°	29°
Footprint across-track (m)	1200	2000	800	1200

placed above the CCD area array. The final result of data acquisition is a data set of overlaid hyperspectral images (Li, Chen, & Baltsavias, 2008), which in general cover the spectral range between 380 and 12,700 nm. Most hyperspectral sensors record the reflected radiation in a series of bands with narrow and continuous wavelength where the number and width of bands varies from one system to another (Vorovencii, 2009).

A hyperspectral sensor widely used in remote sensing is the CASI 1500 (Compact Airborne Spectrographic Imager), developed by Itres Research of Canada. It is a line scanners imager based on a two-dimensional CCD sensor whose instrumental characteristics are reported in Table 6 (De Miguel et al., 2014; Guanter, Estellés, & Moreno, 2007).

The number of spectral bands that can be recorded is strictly connected with the geometric resolution. In particular, the along-track pixel size depends upon the frame rate and the aircraft speed. For example, in order to obtain a GSD of 1 m at flying speed of 120 knots, 36 spectral bands may be acquired. By maintaining the same spatial resolution, but flying at a ground speed of 90 knots, it is possible to acquire 48 bands. Once the pixel size has been chosen, starting from Equation (14) it is possible to compute the flying height above ground:

$$H_g = \frac{c}{p} \cdot \text{GSD}_{ac-tr} \qquad (15)$$

An example of flight planning with CASI 1500 hyperspectral sensor was operated along the coast in the southern part of Italy using a PARTNEAVIA P68 TC Observer aircraft to obtain a *GSD* = 0.6m in spatial mode configuration (Figure 10). Another example of flight planning designed for the HyMap hyperspectral sensor (manufactured by Integrated Spectronics, Australia) over Afghanistan area is described in the paper of Kokaly, King, & Livo, 2008): the flight plan

has been prepared by the software called Survey Planning for Airborne Imaging Spectrometers (SPAIS), a set of custom USGS programs written for the ENVI/IDL software system. The flight plan realized consists in 223 FLs with an along-track pixel size resolution that varies between 24 cm and 37 cm.

Data acquisition

After the selection of the type of sensor to be used for a specific PRS application and the design of the flight plan, the following step to go through is operating data acquisition. During this phase, the management and control of the flight plan is done by the *Flight Management System (FMS) and Control* in manned aircrafts, while in the UAS platforms using the *Ground Control Station (GCS)*.

To ensure the correct data acquisition, it is necessary to check out the quality of GNSS positioning and the weather forecasts before flight operations. The former aspect may be pursued using GNSS mission planning software (see Subsect. 4.1), the latter from the analysis of the METAR information (see Subsect. 4.2).

GNSS visibility planning

GNSS mission planning always plays a key-role, since almost all manned and unmanned aircrafts adopted for PRS missions are equipped with such type of positioning sensors for navigation purpose and, possibly, for direct sensor orientation. Consequently, checking the GNSS satellite visibility is an important task before any missions, but it becomes a particularly critical aspect when integrated GNSS/IMU systems are involved.

In order to obtain centimetre-level accuracy, differential GNSS techniques based on the carrier wavelength (e.g. DGPS) are widely used. The error sources that may

Table 6. Main characteristics of CASI 1500 and HyMap hyperspectral sensors.

Sensor	Focal length (mm)	CCD Pixel sixe (micron)	FOV (deg)	IFOV (Istantaneous Field of view) (mr)	Spatial pixel	Spectral bands	Spectral range (nm)
CASI 1500	40.2	20	40	0.49	1500	288	380–1050
HyMap	–	–	61.3	2.5 (along track) 2.0 (across track)	512	128	450–2480

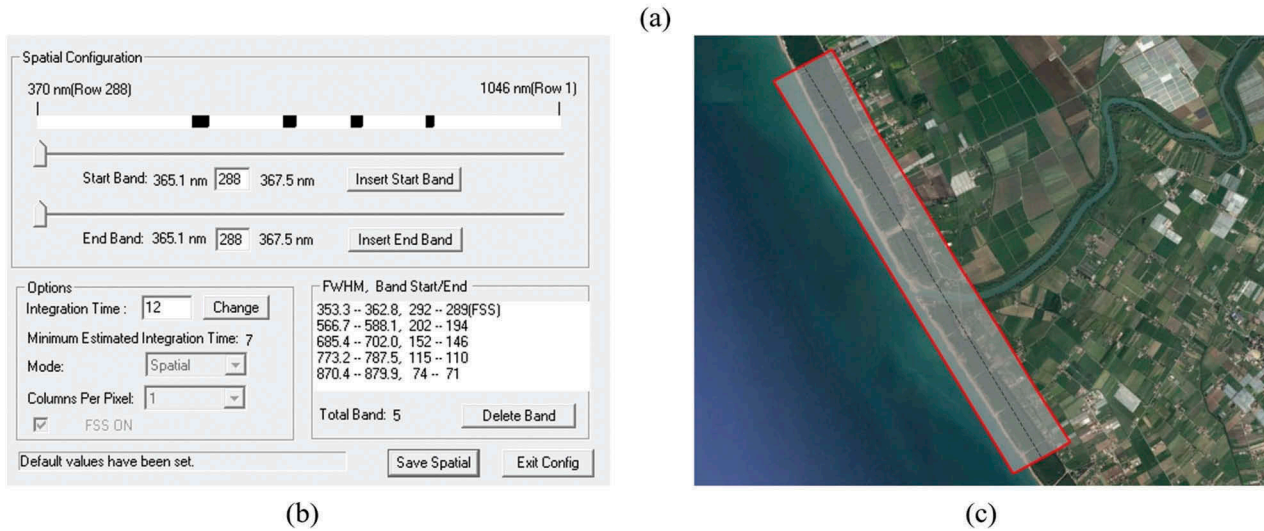| N. bands	IT (ms)	Along-Track Resolution (m)	GS (kt)	(km/h)	Spatial pixel	Swath Width (m)	AGL (m)	ASL (m)
5	12	0.6	97	180	1500	900 m	1200	1200

(a)

(b)

(c)

Figure 10. Flight planning with CASI 1500 hyperspectral sensor over a coastal area in the southern Italy: input parameters (a); spatial configuration (b); footprint of the strip to fly overlaid to an orthophoto (c).

prevent maintenance or re-fixing of integer ambiguities include ionospheric delays, multipaths and poor satellite geometry (Mostafa, Hutton, & Reid, 2001; Xu & Xu, 2016). The latest plays a key role in positioning and may be analysed from satellite ephemeris. Indeed, the *almanac* is a practical and convenient source to get the ephemeris for all the satellites in the constellation. The almanacs are available to users from websites, in the form of a file that is updated almost every day. Two formats are used: SEM (.al3) and YUMA (.alm), see Yuen (2009).

The most common mode for evaluating the quality of positioning depending on a specific satellite constellation is the (PDOP) dilution of precision parameter, which is representative of the relative geometric quality of the satellite constellation, and the number of satellites that can be tracked in a specific time of the day (Hofmann-Wellenhof & Moritz, 2006).

Several software packages are available to work out GNSS visibility planning (Bartoněk & Opatřilová, 2014; Federici, Giacomelli, Sguerso, Vitti, & Zatelli, 2013; Gandolfi & La Via, 2011).

The most software packages for GNSS visibility planning require to input the boundary of the surveyed area and the time window, while they output the geometry of satellite constellations. The presence of obstacles covering the line-of-sight between the receiver and a satellite is not taken into consideration in the most packages. Some of them may also account for a DTM to better refine the GNSS planning. Of course, this problem is effective only in the case of low-height UAS missions and for the master stations that, however, are in general installed in places with an open-sky visibility.

Weather conditions

The atmospheric conditions are a key element for the flight planning of manned and unmanned airborne missions. Indeed, sun lighting, as well as bad weather such as rainfall, crosswinds, fog and clouds might heavily affect the quality of the images (Dandois, Olano, & Ellis, 2015). The analysis of meteorological forecasts in the area of the mission should be carefully analysed, in particular regarding wind speed and direction, wind shear, temperature, precipitation and turbulence. As in the case of manned aircrafts these conditions may only affect the quality of the recorded data, with the exception of very serious weather, in UAS missions also the safety of the vehicle, the payload sensors, and the environment where the flight is operated may be threatened.

Sun-angle height

To ensure a good quality of the recorded images during the mission, it is necessary to guarantee e sufficient illumination of the surveyed scene and to limit the presence of shadows. To this aim, aerial surveys with optical sensors should not be undertaken when the sun angle is less than 30° above the horizon. More in general, the length of the shadows should not exceed 3.5 times the height of the objects (Kraus, 2007). Several tools and software packages allow for the calculation of the height of the sun in relation to the geographical location of the

AOI at a given time. For example: *SolarBeam* (Matusiak, 2008) is a free software for drawing solar path diagrams that also shows the times of sunrise and sunset; *SunEarthTools* (2016) provides a valuable set of online interactive tools that includes modules with which solar sun path charts can be plotted.

During summer, it is also possible to fly under a continuous mantle of clouds at high altitude. This situation is even desirable in dense urban areas to increase the level of detail in dark shadow regions, even if it is quite difficult to obtain homogeneous light conditions. The best period for the photogrammetric aerial survey is essentially based on the ambient light conditions and on the morphological characteristics of the AOI. Therefore, the optimum time for aerial survey is in the central hours of the day where the sun height is greatest. In general, suitable acquisition conditions are obtained with a sun height greater than 30°. In this way, it is possible to obtain bright images and short shades. However, this recommendation is not always valid. Indeed, in spring and summer period, the vegetation can cover the soil details.

Another important issue related to the sun height is the phenomenon called "hot spot". Such an effect leads to a relatively small area that is heavily reflecting sun light, and consequently, may result in an overexposed spots with loss of image detail, especially on water surfaces, wet ground and reflective bodies (such as stained glass and solar panels). Hot spots may be located at the "antisolar point", that is the ground point along the direction between the sun and the sensor, but in the opposite side with respect to the sensor (Tellidis & Levin, 2014). Hot spots are most likely to occur within certain sun-angles, at lower latitude, at higher flight altitudes and with wide-angle lenses (Heath, 1973).

Wind speed and direction

The speed and direction of wind are two weather parameters that may strongly influence the quality of an airborne survey. A twofold reason need to be discussed. The first one concerns the compliance with the designed GSD and, more in general, the compliance of the flight plan in line scanners sensors. The second one concerns the correct acquisition along the designed FLs. Indeed, from Equation (12) it is possible to note that the worst consequence might be in the case of strong wind (or gusts of wind) in transverse direction with respect to the flight direction. To overcome the change of heading of the aircraft, the camera can be rotated in azimuth of an

angle that is approximately equal to the angle of crab. With the use of digital gyro-stabilized mounts installed on modern aerial cameras, the amount of crab, pitch and yaw can be compensated to a certain extent. This is particularly relevant in relation to weather conditions, as they allow image acquisition in more turbulent conditions, especially in large scale, low altitude campaigns. However, because of their high cost, gyro-stabilized mounts are used only in large format DACs. With the explosive growth in the market of small- and medium-format frame cameras, new gyro-stabilized mounts have been designed to accommodate these smaller sensors (Li et al., 2008). Recent studies have shown the full capacity of a three-axis stabilization platform even for an unmanned aircraft photogrammetric systems (Yang, Lin, & Liu, 2016).

Weather condition forecast

Before operating a flight, it is strongly advisable to check the weather conditions. A common approach used in the aviation field consists in consulting the nearest METeorological Aerodrome Report (METAR) station. Through a concise and essential language, METAR shows the following meteorological parameters observed at a given time: wind (direction and intensity), horizontal visibility, visual range of view, ongoing phenomena, cloud cover, air temperature, dew point temperature (useful to derive the relative humidity), and pressure value reduced into standard atmosphere at sea level. The METAR is updated every hour (or fraction of hour, 20 and 50 min) and it is available at every airport (Noaaa, 2016). An example of METAR is reported in Table 7. The content of each field, which is described using a code, is described in the following. It is noteworthy that sometimes not all the components may be present in METAR records Table 8, because at the recording time some data may have not been collected or simply they have been omitted:

(1) International Civil Aviation Organization (ICAO) code station;
(2) Data and time. The letter Z indicates that the reference time frame is UTC (Coordinated Universal Time);
(3) Wind information. The first three digits indicate the true direction, the next two-three digit indicate the speed intensity. Variable direction is indicated by abbreviation VRB. If the wind is greater than three knots and

Table 7. Examples of a METAR (METeorological Aerodrome Report) record describing whether conditions.

	ICAO	Data and time	Wind information	Prevailing Visibility	RVR Weather	Sky condition	Temperature and dew point	Altimeter setting	Remarks
		1	2	3	4	5 6	7	8	9	10
METAR:	LIRF	081450Z	09004KT 060V140	9999		FEW040	14/10	Q1003	NOSIG
METAR:	LIME	151520Z	36010G21KT	2500	4000 +RA	BKN0080	10/10	Q1024	BECMG
METAR:	LIRN	151920Z	VRB02KT			CAVOK	19/16	Q1023	NOSIG

Table 8. Type of sky coverage described on METAR records.

Abbreviation	Meaning
SKC	Sky clear
CLR	No clouds below 12,000 ft (3700 m) (U.S.) or 25,000 ft (7600 m) (Canada)
NSC	"No significant cloud", i.e. none below 5000 ft (1500 m) and no TCU or CB.
CB	"Cumulonimbus cloud"
TCU	"Towering cumulus"
FEW	"Few" = 1–2 oktas cloud coverage
SCT	"Scattered" = 3–4 oktas cloud coverage
BKN	"Broken" = 5–7 oktas cloud coverage
OVC	"Overcast" = 8 oktas, i.e. full cloud coverage
VV	Clouds cannot be seen because of fog or heavy precipitation, so vertical visibility is given instead.
CAVOK	No clouds below 5000 ft, visibility greater than 10 km, absence of fog, rain or snow

Table 9. Details of current FMS/FCMS systems.

FMS/FMCS software package name	Manufacturer
Computer Controlled Navigation System – 5th Generation (CCNS-5)	IGI mbH
Leica FlightPro Flight Management & Control System	Leica Geosysyems
Z/I Inflight	Intergraph®'s Z/I Imaging
SnapSHOT module of X-Track Flight Management Software Suite	Track'Air/Lead'Air Inc
Optech FMS Nav	Teledyne Optech Incorporated
TopoFlight Navigator	TopoFlight Systems

the direction changes more than 60°, it is reported the goniometric range. If there are gusts of wind, the letter "G" is added with the value of wind gusts;

(4) Prevailing Visibility. The visibility is expressed in meters with a four digit number. Four zeros, i.e. "0000" means that visibility is below 50 m, while "9999" means it is above 1 km;

(5) Runway Visual Range (RVR). It represents the real visibility on the runway and it is included in the record only if visibility is inferior to 1,500 m;

(6) Weather and obstructions. The form is a set of two letters for the weather phenomenon, possibly preceded by a descriptor which is also made up of two letters, in turn possibly preceded by an intensity or proximity indicator;

(7) Sky condition. It is the cloud cover present over the airport. In the abbreviation of the METAR, the group is composed of three letters that describe the type of cloud coverage followed by a group of three numbers that indicate the proportion of the clouds above the level of the airport (altitude expressed in hundreds of feet). The amount of clouds is expressed in relation to a unit of measurement called OKTA, which is the amount of clouds equal to the area of 1/8 of the sky within the observer's field of vision. The type of coverage is shown with the codes shown in Table 9. This is one of the most important parameters for the planning PRS missions, because it indicates the possible presence of clouds and their elevation. The ideal condition for the aerial survey is "sky clear – SKC", but also the "1–2 oktas cloud coverage – FEW" status is still a fair condition. In other conditions is not recommended to operate the flight because the probability to find not ideal weather conditions is high;

(8) Temperature and dew point (in degree Celsius);

(9) Altimeter setting. It represents the atmospheric pressure indicated at sea level. It is expressed with four digits preceded by a letter indicating the adopted unit of measurement: hectopascals ("Q") or 1/100 in of mercury ("A"); and

(10) Remarks. This field defines the end of the standard METAR observation record. It may contain some remarks, if necessary. NOSIG appendix indicates that no significant change in the weather is expected in the next two hours.

Further terminology and details can be found in Noaaa (2016). A website where it is possible to see the METAR records from all over the globe is *orbifly.com*.

Flight management system and ground control station

The FMS handles the navigation and the sensor payload during the mission, with the aim of keeping compliance to the designed flight plan. In Figure 11 is shown a sketch of a manned aircraft with the typical position of the FMS's components (FMS control unit, GNSS antenna, IMU, imaging sensor) and their connection scheme.

Therefore, in the case of airborne surveys, the flight crew consists of a pilot, who is responsible for the ordinary navigation, the navigator, who helps the pilot for the detailed navigation, and the operator that controls the sensor payload. During the mission the operator reports the data information (number of strips, presence of clouds on photos, problems with GNSS positioning, etc.) on flying reports which may depend upon the sensor type.

In order to fully integrate the navigation system with the direct orientation GNSS/IMU unit, some manufacturers have created a unique FMS that concurrently controls both of them. A further step is represented by FCMS (Flight Management and Control System) which also may control the sensor for data acquisition. An example of FCMS is the Applanix POSTrack™, which is the first fully integrated, real-time direct georeferencing and FMS designed for the airborne geospatial community (Ip,
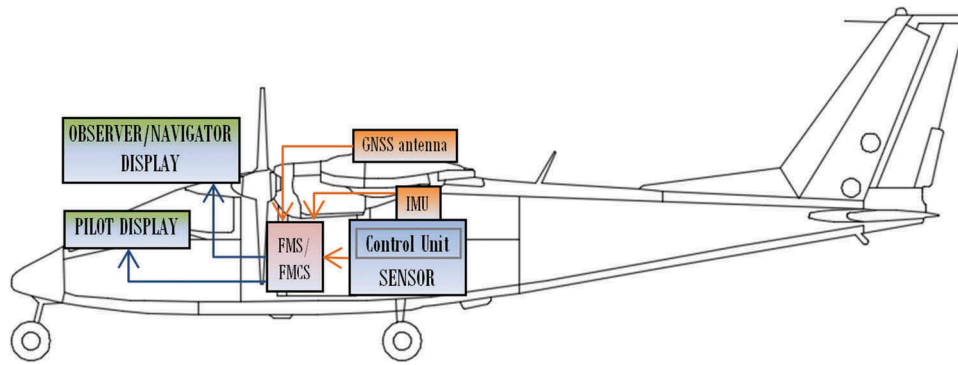
Figure 11. Connection diagram of the FMS sketched on a Partenavia P68 aircraft.
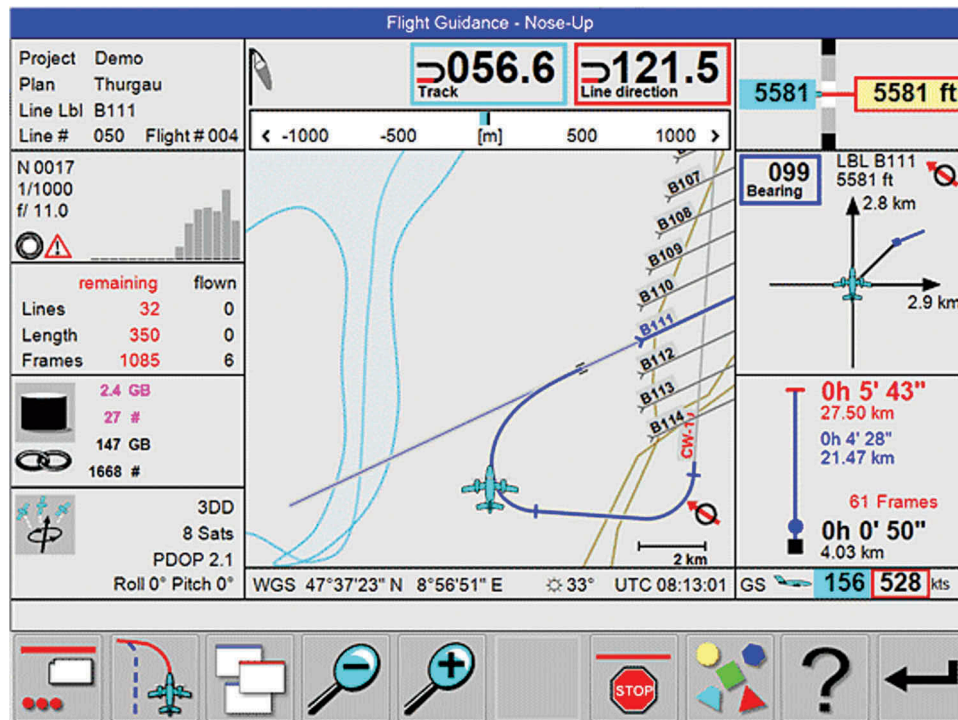

Figure 12. Screen shot of Leica Geosystems FlightPro Flight Management & Control System in "Nose-up" view mode (Leica Geosystems, 2017).

Mostafa, Huttona, & Barriere, 2008). Another example of FCMS system is Leica Geosystems FCMS™ (Zuberbühler & Fricker, 2004), which may take care of the following tasks using a single interface: flight guidance, sensor release and sensor monitoring. The latest version released by this company is the FlightPro Flight Management and Control System. In this environment, during flight execution, the operator and the pilot can independently select various views. The optimized flight guidance offers north-up views for project overview and control of the flight operation progress. The "Nose-up" view (Figure 12) suggests the optimized flight path, and the in-line view helps precise navigation along the planned FL.

Several FMS software packages also incorporate a video camera to facilitate and enhance the ability to sensor control. Indeed, the chance to watch below the aircraft allows to check the presence of clouds, flue or other obstacles that may hinder the correct data acquisition. A list of some FMS/FCMS systems and their relative manufactures is shown in Table 9.

In UAS environment, the flight planning operation is controlled by the GCS, see Hong, Fang, and Tao (2008). A GCS may control several tasks, such as launch, landing, flight and recovery of the flying vehicle, emergency situations, communication with payload sensors, and acts as interface between the UAS system and the outside world (Thru, 1999). In general, the GCS may be installed on a dedicated remote controller, even though a major popularity has been gained by software implementations on laptops, smartphones and tablets (Natarajan, 2001). The tendency is to embed the control of either the sensors and the navigation within a unique GCS, so that all tasks may be integrated into the same tool. The technology is in continuous and fast development, thus it is very difficult to define a consolidated state-of-the-art.
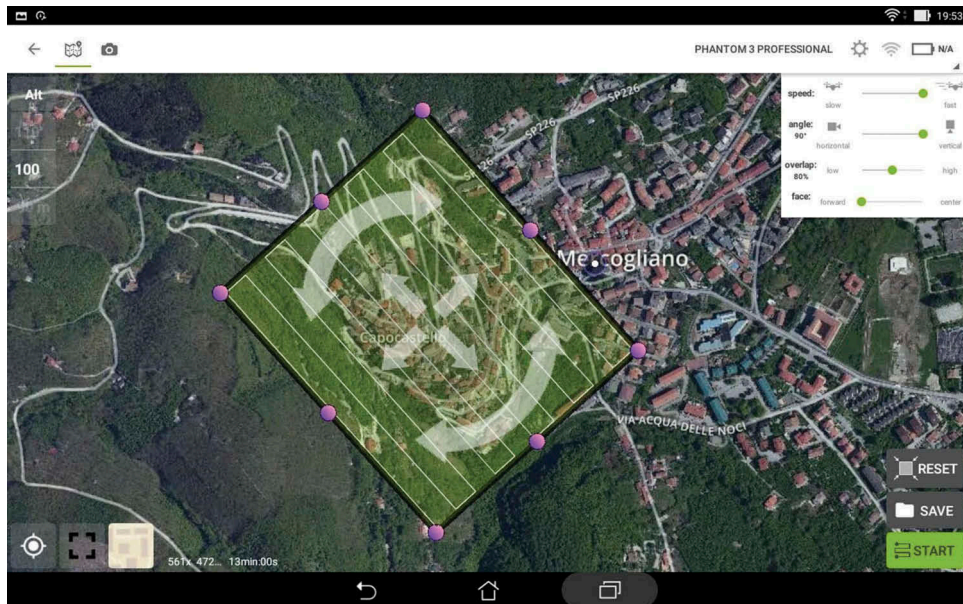
Figure 13. Screen shoot of the mission planning in Pix4Dcapture GCS, which can be installed on a tablet.

Figure 13 shows a screenshot of the GCS system of *Pix4Dcapture* environment (Pix4D, 2016) during the operation of a flight with a digital frame camera. This software runs on a tablet.

Designing flight route

In order to cover the AOI of the project by flying more strips, if required by the project's extension, the choice of the flight direction is a crucial aspect that may be based on the following criteria:

– Uniform lighting and orientation of the block along the East-West direction, in order to minimize the effect of shadows;
– Shape of the AOI: the direction of strips is orientated along the longer dimension of the AOI; and
– Local topography.

Of course, also the mutual positions of the strips should be carefully organized to obtain the planned sidelaps.

After the general layout of the strips is planned, the direction of single strips has to be identified. Depending on the flight route, different schemes (Mah &

Cryderman, 2015; Gandor, Rehak, & Skaloud, 2015) may be implemented as shown in Figure 14:

(a) strips alternatively flown in opposite directions ("zig-zag" scheme);
(b) a group of strips is flown only in one direction, followed by another group in the opposite direction ("jump line" scheme); and
(c) all strips flown along the same direction ("one way" or "racetrack" scheme).

The choice of a scheme may influence either the quality of a survey and the budgetary aspects, as well as the efficiency of the project. The scheme to adopt does not depend upon the automation of the adopted navigation system, but upon the aircraft's characteristics (rotary ore fixed wing) and the type of the payload sensor. In the case of manned fixed-wing aircrafts equipped with a direct orientation GNSS/IMU system, the "jump line" scheme should be preferred as it is more efficient. Indeed, the aircraft takes less time to intercept the several strips and, moreover, in the case of manned aerial survey, this scheme allows the pilot to turn the plane comfortably in the same direction. In aerial surveys operated with rotary-wing aircrafts, the most efficient flight plan is based on a "zig-zag" scheme, because it allows to fly adjacent strips in shorter time. Indeed, the time elapsed during the
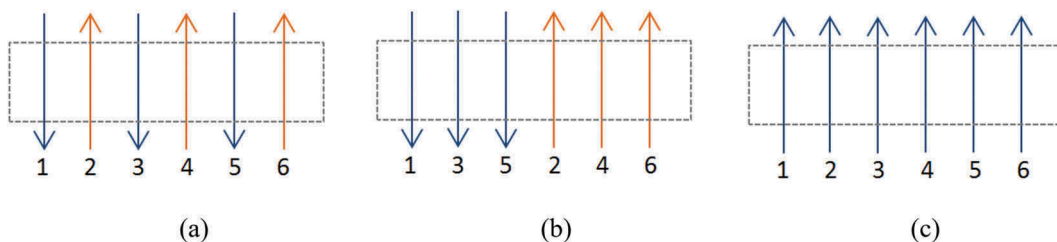

Figure 14. Possible acquisition schemes for aerial photogrammetry missions: "zig-zag" (a); "jump line" (b); "one way" or "racetrack" (c).

mission is a critical parameter in the case of UAS's, because it cannot be longer of the battery supply. In addition, the "zig-zag" scheme is used for the calibration of the integrated system including imaging and GNSS-IMU sensors (boresight misalignment). Instead, the "one way" scheme is preferable when using hyperspectral sensors (disregarding if it is operated with rotary or with fixed-wing aircrafts).

Conclusions

An overview on the mission planning obtainable by the most recent platform and sensors for PRS purpose has been presented. While in the past the most common way to know the correct flying height was to choose the scale of the map and consequently the scale of the frame (using the Von Gruber's formula), the advent of digital technology has radically changed this approach. Indeed, the choice of a type of a sensor may vary the characteristics of the flight planning (flight height, footprint, overlap, etc.). In the case of frame digital camera sensors, once the characteristics of the sensor are known, the flight planning parameters can be determined by Equation (4). These parameters are independent (excluding the frame rate) of the aerial platform type. Instead, in the photogrammetric and hyperspectral line scanners sensors, the flight planning parameters are function, beyond the intrinsic characteristics of the adopted sensor (focal and pixel size), even of the type of aerial platform and the environment conditions of the survey mission, such as the wind speed. Furthermore, in this latter type of sensors a key role for a successful aerial survey is represented of the determination of the EO parameters on the basis of GNSS/IMU systems. Also, in order to obtain a good accuracy, the mission planning must be carefully prepared considering the satellite configuration and the most suitable flight route.

Moreover, thanks to advances in microelectronics and nanotechnology, new light and small sensors have been developed to acquire images with high geometric and radiometric resolution, also in multispectral and hyperspectral mode. This ability has allowed to adapt them very well to UAV platforms. Indeed, the trend of the survey with these aerial platforms is increasing, especially for small projects (e.g. in the field of cultural heritage conservation, precision agriculture and the like).

As far as it concerns the software packages for flight planning, while in the past they were strictly connected to specific sensor types and models, the introduction of open-source software by UAS systems has led to a new approach to photogrammetric sector of the mission planning. Increasingly, these types of software packages allow to manage different types of sensors (in general featuring a small frame), mainly dedicated to the use of UAV platforms. Therefore, the development open-source software that allow even the management of oblique frame camera and line scanners sensors is desirable in the future.

Lastly, it is still important to describe on a flight report the several items of information related to acquisition data operations, such as the number of strips and frames acquired of a specific job, the crew, the type of aerial platform and potential problems (GNSS gaps data, presence of clouds, troubles to the sensor). Depending on the type of sensor, two examples of flight reports can be constructed, as shown in Appendix A.

Disclosure statement

No potential conflict of interest was reported by the authors.

ORCID

Massimiliano Pepe http://orcid.org/0000-0003-2508-5066
Marco Scaioni http://orcid.org/0000-0003-4058-6176

References

Aggarwal, S. (2004, July 7–11). Principles of remote sensing. In M.V.K. Sivakumar, P.S. Roy, K. Harmsen, & S.K. Saha (Eds.), *Satellite remote sensing and GIS applications in agricultural meteorology* (pp. 23–38). Dehra Dun: World Meteorological Organisation, Switzerland.

Alba, M., Barazzetti, L., & Scaioni, M. (2011). Filtering vegetation from terrestrial point clouds with low-cost near infrared cameras. *The Italian Journal of Remote Sensing*, 43(2), 55–75.

Baltsavias, E.P. (1999). A comparison between photogrammetry and laser scanning. *ISPRS Journal of Photogrammetry and Remote Sensing*, 54(2), 83–94.

Barazzetti, L., Forlani, G., Remondino, F., Roncella, R., & Scaioni, M. (2011, May 23–26). Experiences and achievements in automated image sequence orientation for close-range photogrammetric projects. In F. Remondino & M.R. Shortis (Eds.), *Proceedings of International Confonference "Videometrics, Range Imaging, and Applications XI", Proceedings of SPIE, paper No. 80850F* (Vol. 8085, p. 13 (e-doc)). Munich. doi:10.1117/12.890116

Barazzetti, L., Remondino, F., & Scaioni, M. (2010). Automation in 3D reconstruction: Results on different kinds of close-range blocks. *International Archives*

Photogramm Remote Sensing Spatial Information Sciences, 38(5), 55–61.

Barnard, J. (2007).*Small UAV (<150 kg TOW) command, control and communication issues* (Technical Report). Institution of Engineering and Technology.

Bartoněk, D., & Opatřilová, I. (2014). The use of GIS technology for planning of GNSS measurement. *Advances in Intelligent Systems*, 53, 281–294.

Barzaghi, R., Carrion, D., Pepe, M., & Prezioso, G. (2016). Computing the deflection of the vertical for improving aerial surveys: A comparison between EGM2008 and ITALGEO05 Estimates. *Sensors*, 16(8), 1–12, 1168.

Budzier, H., & Garlach, G. (2011). *Thermal infrared sensors, theory, optimization and practice* (p. 302). Chichester, UK: John Wiley & Sons.

Bühler, Y., Marty, M., Egli, L., Veitinger J., Jonas T., Thee P., & Ginzler C. (2015). Snow depth mapping in high-alpine catchments using digital photogrammetry. *Cryosphere*, 9 (1), 229–243.

Canon. (2016). *Technical specifications*. Retrieved August 31, 2017, from https://www.usa.canon.com/internet/portal/us/home/support/details/cameras/support-dslr/eos-5d-mark-ii/eos-5d-mark-ii#technicalspecifications_tab

Cheak, S. F. (2004).Detecting near-UV and near-IR wavelengths with the FOVEON image sensor (Doctoral dissertation, Monterey California. Naval Postgraduate School).

Clapuyt, F., Vanacker, V., & Van Oost, K. (2016). Reproducibility of UAV-based earth topography reconstructions based on Structure-from-Motion algorithms. *Geomorphology*, 260, 4–15.

Cocks, T., Jenssen, R., Stewart, A., Wilson, I., & Shields, T. (1998, October 6-8). The HyMapTM airborne hyperspectral sensor: The system, calibration and performance. In *Proceedings of the 1st EARSeL workshop on Imaging Spectroscopy* (pp. 37–42). Zurich.

Colomina, I., & Molina, P. (2014). Unmanned aerial systems for photogrammetry and remote sensing: A review. *ISPRS Journal of Photogrammetry and Remote Sensing*, 92, 79–97.

Cramer, M. (2003). Integrated GPS/inertial and digital aerial triangulation–Recent test results. In D. Fritsch (Ed.), *Photogrammetrische Woche 2003* (Vol. 3, pp. 161–172). Heidelberg: Wichmann Verlag.

Cramer, M., Stallmann, D., & Haala, N. (2000). Direct georeferencing using GPS/inertial exterior orientations for photogrammetric applications. *International Archives Photogramm Remote Sensing Spatial Information Sciences*, 33(B3/1), 198–205.

Dandois, J.P., Olano, M., & Ellis, E.C. (2015). Optimal altitude, overlap, and weather conditions for computer vision UAV estimates of forest structure. *Remote Sensing*, 7(10), 13895–13920.

De Miguel, E., Fernández-Renau, A., Prado, E., Jiménez, M., De la Cámara, Ó.G., Linés, C., & Muñoz, F. (2014). The processing of CASI-1500I data at INTA PAF. *EARSeL eProceedings*, 13(1), 30–37.

Degnan, J.J., & Field, C.T. (2014). Moderate to high altitude, single photon sensitive, 3D imaging lidars. *SPIE Sensing Technology Applications*, 9114, 91140H.

Dell'Endice, F. (2008, July 3–11). Improving the performance of hyperspectral pushbroom imaging spectrometers for specific science applications. In *International Society for Photogrammetry and Remote Sensing* (Vol. XXXVII Part B7, pp. 215–220). Beijing.

Dold, J., & Flint, D. (2007). Leica geosystems photogrammetric sensor and workflow developments. In D. Fritsch (Ed.), *Photogrammetrische Woche 2007* (Vol. 1, pp. 3–14). Heidelberg: Wichmann Verlag.

Dorrington, A.A., Payne, A.D., & Cree, M.J. (2010). An evaluation of time-of-flight range cameras for close range metrology applications. *International Archives Photogramm Remote Sensing Spatial Information Sciences*, XXXVIII(Part 5), 201–206.

Ebadi, H. (2006). *Advanced analytical aerial triangulation*. KN Toosi University of Technology.

Eisenbeiss, H. (2009). *UAV photogrammetry* (Ph.D. Thesis). Institut für Geodesie und Photogrammetrie, ETH, Zürich.

Eisenbeiss, H., & Sauerbier, M. (2011). I*nvestigation of UAV systems and flight modes for photogrammetric applications*. The Photogrammetric Record, 26(136), 400–421.

El-Hakim, S., Beraldin, J., & Blais, F. (2003, September 22–25). Critical factors and configurations for practical 3D image-based modeling. In *Proceedings of the 6th Conference on Optical 3D Measurements Techniques* (Vol. 2, pp. 159–167). Zurich.

Eling, C., Klingbeil, L., & Kuhlmann, H. (2015). Real-time single-frequency GPS/MEMS-IMU attitude determination of lightweight UAVs. *Sensors*, 15(10), 26212–26235.

Everaerts, J. (2009). *New platforms - unconventional platforms (unmanned aircraft systems) for remote sensing* (p. 102). EuroSDR Official Publication, No. 56.

Federici, B., Giacomelli, D., Sguerso, D., Vitti, A., & Zatelli, P. (2013). A web processing service for GNSS realistic planning. *Applied Geomatics*, 5(1), 45–57.

Filippone, A. (2008). Comprehensive analysis of transport aircraft flight performance. *Progress in Aerospace Sciences*, 44(3), 192–236.

Förstner, W. (1985). The reliability of block triangulation. *Photogrammetric Engineering & Remote Sensing*, 51(6), 1137–1149.

Fowler, J.E. (2014, October 27–30). Compressive pushbroom and whiskbroom sensing for hyperspectral remote-sensing imaging. In *Proc. 2014 IEEE International Conference on Image Processing (ICIP)* (pp. 684–688). Paris: CNIT La Defense.

Fraser, C.S. (1996). *Network design. Close range photogrammetry and machine vision* (pp. 256–281). Caithness: Whittles Publishing. (Ed. K.B. Atkinson).

Gandolfi, S., & La Via, L. (2011). SKYPLOT_DEM: A tool for GNSS planning and simulations. *Applied Geomatics*, 3(1), 35–48.

Gandor, F., Rehak, M., & Skaloud, J. (2015, August 30–September 2). Photogrammetric mission planner for Rpas. *International Archives Photogramm Remote Sensing Spatial Information Sciences*, 40(1), 61–65. Toronto.

Georgi, C., Stognienko, R., Knuth, S., & Albe, G. (2005). JAS The next generation digital aerial scanner. In D. Fritsch (Ed.), *Photogrammetrische Woche 2005* (pp. 147–154). Heidelberg: Wichmann Verlag.

Gomarasca, M.A. (2009). *Basics of geomatics* (pp. 316–320). Springer Science & Business Media.

Grenzdörffer, G. (2010). *Medium format cameras* (pp. 233–262). EuroSDR Official Publication, No. 58.

Gruber, M., & Walcher, W. (2014, February 12-14). Calibrating the new Ultracam Osprey oblique aerial sensor. *International Archives Photogramm Remote Sensing Spatial Information Sciences*, 40(3). 47–52. Castelldefels, Spain.

Grubera, M., Perkob, R., & Ponticellia, M. (2004, July 12–23). The all digital photogrammetric workflow: Redundancy and robustness. In *International archives of the photogrammetry, remote sensing and spatial information sciences* (Vol. XXXPart B1, pp. 232–234). Istanbul.

Grun, A., & Zhang, L. (2002). Automatic DTM generation from three-line-scanner (TLS) images. *International Archives Photogramm Remote Sensing Spatial Information Sciences*, 34(3/A), 131–137.

Guanter, L., Estellés, V., & Moreno, J. (2007). Spectral calibration and atmospheric correction of ultra-fine spectral and spatial resolution remote sensing data. *Application to CASI-1500 Data. Remote Sensing of Environment*, 109(1), 54–65.

Haala, N., Fritsch, D., Stallmann, D., & Cramer, M. (2000). On the preformance of digital airborne pushbroom cameras for photogrammetric data processing-a case study. *International Archives Photogramm Remote Sensing Spatial Information Sciences*, 33(B4/1), 324–331.

Heath, G.R. (1973). Hot spot determination. *Photogrammetric Engineering*, 39, 1205–1214.

Heipke, C., & Eder, K. (1998). *Performance of tie-point extraction in automatic aerial triangulation* (pp. 125–185). OEEPE Official Publications, No. 35. Germany.

Hofmann-Wellenhof, B., & Moritz, H. (2006). *Physical geodesy*. Vienna: Springer-Verlag.

Höhle, J. (2008). Photogrammetric measurements in oblique aerial images. *Photogrammetrie Fernerkundung Geoinformation*, 1, 7–14.

Hong, Y., Fang, J., & Tao, Y. (2008). Ground Control Station development for autonomous UAV. *Intelligent Robotics and Applications*, 5315/2008, 36–44.

Höhle, J. (2011). DEM generation by means of new digital aerial camera. *International Archives Photogramm Remote Sensing Spatial Information Sciences*, 38(3/W22), 185–190.

Ip, A.W.L., Mostafa, M.M.R., Huttona, J., & Barriere, J.P. (2008). An optimally integrated direct georeferencing and flight management system for increased productivity of airborne mapping and remote sensing. *International Archives Photogramm Remote Sensing Spatial Information Sciences*, 37(B1), 579–584.

Jacobsen, K. (2010, October 11–13). Development of digital aerial cameras. *International Archives Photogramm Remote Sensing Spatial Information Sciences*, XXXVIII-1/W17, 11–13. Turkey.

Jacobsen, K., & Gerke, M. (2016). Sub-camera calibration of a penta-camera. *International Archives of the Photogrammetry, Remote Sensing and Spatial Information Sciences*, XL-3/W4, 35–40.

Jarvis, A., Reuter, H.I., Nelson, A., & Guevara, E. (2008). *Hole-filled SRTM for the globe Version 4*. Retrieved from the CGIAR-CSI SRTM 90m Database http://srtm.csi.cgiar.org

Kemper, G. (2012). New airborne sensors and platforms for solving specific tasks in remote sensing. *International Archives Photogramm Remote Sensing Spatial Information Sciences*, XXXIX-B5, 351–356.

Kokaly, R.F., King, T.V., & Livo, K.E. (2008). *Airborne hyperspectral survey of Afghanistan 2007: Flight line planning and HyMAP data collection*. US Geological Survey.

Kraus, K. (2007). *Photogrammetry: Geometry from Images and Laser, Scans* (2nd ed., p. 459). Germany: Walter de Gruyter.

Kremer, J., & Gruber, M. (2004). Operation of the UltraCamD together with CCNS4/Aerocontrol–First experiences and results. *International Archives Photogramm Remote Sensing Spatial Information Sciences*, XXXV Part B1, 172–177.

Kumar, S. (2005). *Basics of remote sensing and GIS* (pp. 64–65). New Delhi: Firewall Media.

Leica FlightPro Flight Management & Control System. (2017). Retrieved January 16, 2017, from http://leica-geosystems.com/products/airborne-systems/software/leica-flightpro

Lemmens, M.J.P.M. (2014). *Digital oblique aerial cameras (1): A survey of features and systems*. Netherlands: GIM International.

Li, Z., Chen, J., & Baltsavias, E. (2008). *Advances in photogrammetry, remote sensing and spatial information sciences: 2008 ISPRS congress book* (Vol. 7, pp. 153–155). Bristol, PA: Taylor & Francis.

Luhmann, T., Robson, S., Kyle, S., & Boehm, J. (2013). *Close range photogrammetry: 3D imaging techniques* (p. 684). Berlin: Walter De Gruyter Inc.

Luhmann, T., Robson, S., Kyle, S., & Boehm, J. (2014). *Close range photogrammetry: 3D imaging techniques* (2nd ed., p. 684). Germany: Walter De Gruyter Inc.

Madani, M. (2012, August 25–September 1). Accuracy potential and applications of MIDAS aerial oblique camera system. In *International archives of the photogrammetry, remote sensing and spatial information sciences* (Vol. 39, pp. 127–132). Melbourne.

Madani, M., & Mostafa, M.M.R. (2001). ISAT direct exterior orientation QA/QC strategy using POS data. In *Proceedings of OEEPE workshop: Integrated sensor orientation* (pp. 17–18). Hanover.

Mah, S.B., & Cryderman, C.S. (2015, August 30–September 2). Implementation of AN unmanned aerial vehicle system for large scale mapping. In *International archives of the photogrammetry, remote sensing and spatial information sciences* (Vol. XL-1/W4, pp. 47–54). Toronto.

Mallaun, C., Giez, A., & Baumann, R. (2015). Calibration of 3-D wind measurements on a single-engine research aircraft. *Atmospheric Measurement Techniques*, 8(8), 3177–3196.

Matusiak, B. (2008, December 4–5). The graphical tool for sky component, solar glare and overheating risk prediction, proceedings of SOLARIS 2008. In *4th international conference on solar radiation & daylighting*. Hong Kong.

Mesas-Carrascosa, F.J., Rumbao, I.C., Berrocal, J.A.B., & Porras, A.G.F. (2014). Positional quality assessment of orthophotos obtained from sensors onboard multi-rotor UAV platforms. *Sensors*, 14(12), 22394–22407.

Mian, O., Lutes, J., Lipa, G., Hutton, J.J., Gavelle, E., & Borghini, S. (2015). Direct georeferencing on small unmanned aerial platforms for improved reliability and accuracy of mapping without the need for ground control points. In *The international archives of photogrammetry, remote sensing and spatial information sciences* (Vol. XL-1/W4, pp. 397–402).

Microdrones. (2017). Retrieved January 2, 2017, from https://www.microdrones.com/fileadmin/web/Images/produkte/md4-1000/md4-1000-flyer_EN.pdf

Microsoft, U. (2016). *Technical specifications*. Retrieved November 11, 2016, from http://www.kasurveys.com/documents/UltraCamEagle-Specs.pdf

Mikhail, E., Bethel, J., & McGlone, J. (2001). *Introduction to modern photogrammetry* (p. 496). New York: John Wiley & Sons.

Möllney, M., & Kremer, J. (2013). Contour flying for airborne data acquisition. *In Photogrammetric Week*, 13, 117–129.

Morgan, D., & Falkner, E. (2001). *Aerial mapping: Methods and applications* (pp. 35–36). Boca Raton, FL: CRC Press.

Mostafa, M., Hutton, J., & Reid, B. (2001, September). GPS/IMU products-the Applanix approach. *Photogrammetric Week*, 1, 63–83.

Mostafa, M.M. (2001, June). Boresight calibration of integrated inertial/camera systems. In *Proceedings of the international symposium on kinematic systems in geodesy, geomatics and navigation (KIS 2001)* (pp. 5–8). Banff, AB.

Mostafa, M.M. (2002). Precision aircraft GPS positioning using CORS. *Photogrammetric Engineering & Remote Sensing*, 68(11): 1125–1126.

Natarajan, G. (2001). Ground control stations for unmanned air vehicles. *Defence Science Journal*, 51(3), 229–237.

Neumann, K., Welzenbach, M., & Timm, M. (2016). *CMOS imaging sensor technology for aerial mapping cameras. International Archives Photogramm Remote Sensing Spatial Information Sciences*, 41(B1), 69–72.

Neumann, K.J. (2004). Operational aspects of digital aerial mapping cameras. *The International Archives of the Photogrammetry, Remote Sensing and Spatial Information Sciences*, 35(B1), 222–225.

Neumann, K.J. (2005). *Digital aerial cameras* (pp. 1–5). Germany: Intergraph Z/I Deutschland GMBH.

Nex, F., & Remondino, F. (2014). UAV for 3D mapping applications: A review. *Applied Geomatics*, 6, 1–15.

Noaaa. (2016). *Aviation weather observations for supplementary aviation weather reporting stations (sawrs) manual observations*. Retrieved November 30, 2016, from http://www.nws.noaa.gov/os/coop/Publications/WSOH8.pdf

Oborne, M. (2013). *Mission planner*. Software. Retrieved May 18, 2017, from http://ardupilot.org/planner/

Orbifly. (2016). Retrieved November 30, 2016, from http://www.orbifly.com/member/metmap.php

Pepe, M., & Prezioso, G. (2015). A matlab geodetic software for processing airborne LIDAR bathymetry data. *The International Archives of Photogrammetry, Remote Sensing and Spatial Information Sciences*, 40(5), 167.

Pepe, M., & Prezioso, G. (2016). Two approaches for dense DSM Generation from Aerial Digital Oblique Camera System. In *Proceedings of the 2nd international conference on geographical information systems theory, applications and management*, Rome, Italy, 26–27 April 2016; (pp. 63–70).

Pepe, M., Prezioso, G., & Santamaria, R. (2015). Impact of vertical deflection on direct georeferencing of airborne images. *Survey Review*, 47(340), 71–76.

Petrie, G. (2009). Systematic oblique aerial photography using multiple digital cameras. *Photogrammetric Engineering & Remote Sensing*, 75(2), 102–107.

Petrie, G., & Walker, A.S. (2007). Airborne digital imaging technology: A new overview. *The Photogrammetric Record*, 22(119), 203–225.

Phase One Industrial. (2016). *Technical specifications*. Retrieved December 30, 2017, from http://industrial.phaseone.com/iXU_camera_system.aspx

Photometrics. (2017). *New-generation CCD/EMCCD technology. A review of eXcelon™ technology* (Technical Note). Retrieved January 20, 2018, from https://www.photometrics.com/resources/technotes/pdfs/eXcelon-TechNote.pdf

Pix4D. (2016). *Ground control system*. Retrieved from www.pix4d.com

Planner, M. (2016). *Open source ground station*. Retrieved November 30, 2016, from http://ardupilot.org/

Ringaby, E., Friman, O., Forssén, P.E., Opsahl, T.O., Haavardsholm, T.V., & Kasen, I. (2014). Anisotropic scattered data interpolation for pushbroomimage rectification. *IEEE Transactions on Image Processing*, 23(5), 2302–2314.

Rizaldy, A., & Firdaus, W. (2012). Direct georeferencing: A new standard in photogrammetry for high accuracy mapping. *Proceedings of International Archives of the Photogrammetry, Remote Sensing and Spatial Information Sciences*, 39(B1), 5–9.

Rupnik, E., Nex, F., & Remondino, F. (2014). Oblique multi-camera systems – Orientation and dense matching issues. *International Archives of Photogrammetry, Remote Sensing and Spatial Information Sciences*, 40(3/W1), 107–114.

Schiele, O., Kleusberg, A., & Horn, R. (2002, May). A comparison of two integrated airborne positioning and orientation systems. In *Proceedings of the 9th Saint Petersburg international conference on integrated navigation systems* (pp. 27–29).

Schwarz, K.P. (1996). Aircraft position and attitude determination by GPS and INS. *International Archives of Photogrammetry and Remote Sensing*, 31, 67–73.

Semanjski, S., Dubravko, G., & Hrvoje, G. (2008). GPS aided INS-integration and application in the croatian sky. In *1st GNSS vulnerabilities and solutions conference*.Baška, Croatia.

Shan, J., & Toth, C.K. (2009). *Topographic laser scanning and ranging. Principles and processing*. Boca Raton, FL: Taylor and Francis Group.

Snavely, N. (2008). *Scene reconstruction and visualization from Internet photo collections* (Unpublished PhD thesis, University of Washington, USA).

Sun Earth Tools-sun position. (2016). Retrieved November 30, 2016, from http://www.sunearthtools.com/dp/tools/pos_sun.php?lang=it

Tellidis, I., & Levin, E. (2014). Photogrammetric image acquisition with small unmanned aerial systems. In *ASPRS 2014 annual conference Louisville*. Kentucky.

Thomas, T., & Gray, H. (2016). *Green Falcon IV: An unmanned aerial system and an integrated wireless sensor network for remote sensing tasks* (pp. 1–32). ePrints.

Thru, A. (1999). This paper is part of the following report: Title. *Advances in Vehicle Systems Concepts and Laser*, 16(1), ADP010339.

Toth, C.K. (2001). Sensor integration in airborne mapping. In *Instrumentation and Measurement Technology Conference, 2001. IMTC 2001. Proceedings of the 18th IEEE* (Vol. 3, pp. 2000–2005). IEEE.

U.S. Department of Transportation. (2013). *Federal Aviation Administration Integration of Civil Unmanned Aircraft Systems (UAS) in the National Airspace System (NAS) Roadmap*.

Van der Meer, F.D., Van der Werff, H.M., van Ruitenbeek, F.J., Hecker, C.A., Bakker, W.H., Noomen, M.F., … Woldai, T. (2012). Multi- and hyperspectral geologic remote sensing: A review. *International Journal of Applied Earth Observation and Geoinformation*, 14, 112–128.

Varshney, P.K., & Arora, M.K. (2004). *Advanced image processing techniques for remotely sensed hyperspectral data*. Germany: Springer Science & Business Media.

Vorovencii, I. (2009). The hyperspectral sensors used in satellite and aerial remote sensing. *Bulletin of the Transilvania University of Brașov*, 2(Series II), 51–56.

Vosselman, G., & Maas, H.G. (2010). *Airborne and terrestrial laser scanning* (p. 320). Boca Raton, FL: Taylor and Francis Group.

Wagner, W., Blöschl, G., Pampaloni, P., Calvet, J.C., Bizzarri, B., Wigneron, J.P., & Kerr, Y. (2007). Operational readiness of microwave remote sensing of soil moisture for hydrologic applications. *Hydrology Research*, 38(1), 1–20.

Wang, M., Hu, J., Zhou, M., Li, J.M., & Zhang, Z. (2013). Geometric correction of airborne linear array image based on bias matrix. *International Archives of the Photogrammetry, Remote Sensing and Spatial Information Sciences*, 40(1/W1), 369–372.

Wegmann, H. (2002). Image orientation by combined (A) AT with GPS and IMU. *International Archives Of Photogrammetry Remote Sensing And Spatial Information Sciences*, *34*(1), 278–283.

Wehrli, H., Gayda, V., Wehrli, G., & BeThel, J. (2004). Introduction of the 3-Das-1 digital aerial scanner. *International Archives of the Photogrammetry, Remote Sensing and Spatial Information Sciences*, *35*(B1), 561–564.

Westoby, M.J., Brasington, J., Glasser, N.F., Hambrey, M.J., & Reynolds, J.M. (2012). Structure-from-Motion'photogrammetry: A low-cost, effective tool for geoscience applications. *Geomorphology*, *179*, 300–314.

Xu, G., & Xu, Y. (2016). Applications of GPS theory and algorithms. In *GPS* (pp. 313–340). Germany: Springer Berlin Heidelberg.

Yang, Y., Lin, Z., & Liu, F. (2016). Stable imaging and accuracy issues of low-altitude unmanned aerial vehicle photogrammetry systems. *Remote Sensing*, *8*(4), 316.

Yuen, M.F. (2009). *Dilution of precision (DOP) calculation for mission planning purposes* (Doctoral Dissertation, Naval Postgraduate School, Monterey, CA.

Yundong, W.U., Qiang, Z., & Shaoqin, L. (2008). A contrast among experiments in three low-altitude unmanned aerial vehicles photography: Security, quality & efficiency. *International Archives of the Photogrammetry, Remote Sensing and Spatial Information Sciences*, *37*(B1), 1223–1227.

Zhang, A., Hu, S., Meng, X., Yang, L., & Li, H. (2015). Toward high altitude airship ground-based boresight calibration of hyperspectral pushbroom imaging sensors. *Remote Sensing*, *7*(12), 17297–17311.

Zuberbühler, F., & Fricker, P. (2004). Distance learning of FCMS. The Leica Flight & Sensor Control Management System. *International Archives of the Photogrammetry, Remote Sensing and Spatial Information Sciences*, *35*(B6), 1–3.

Appendix A

FLIGHT REPORT FOR DIGITAL FRAME CAMERA SENSOR

Order number		Date Of The Flight		□ CORS		
Project name		Take Off Position	Landing Position	□ GNSS base		
Location				IMU	Start	Stop
		Take Off Time	Landing Time			
Pilot				Lever Arm		
Navigator		□ Aircraft	Model	X	Y	Z
Observer		□ Helicopter				
		□ UAS		Boresight misalignment		
Weather Condition		Sensor (or sensors) name		Omega	Phi	Kappa
METAR:						

N.	Photo (from – to)	Direction	Start	Stop	Note

FLIGHT REPORT FOR LINE SCANNERS SENSORS

Order number		Date Of The Flight		□ CORS		
Project name		Take Off Position	Landing Position	□ GNSS base		
Location				IMU	Start	Stop
Pilot		Take Off Time	Landing Time			
Navigator				Lever Arm		
Observer		□ Aircraft	Model	X	Y	Z
Weather Condition		□ Helicopter				
METAR:		□ UAS		Boresight misalignment		
	Ground	In fly	Sensor (or sensors) name	Omega	Phi	Kappa
Temperature						
Pressure			Ground speed <			

N. Strip	Direction	Start	Stop	Note